High-resolution imaging of presynaptic ER networks in *Atlastin* mutants

Mónica C. Quiñones-Frías[1], Dina M. Ocken[1] and Avital Rodal[1,*]
[1]Department of Biology, Brandeis University, Waltham, MA
*Corresponding author:
Email: arodal@brandeis.edu

Abstract:

The endoplasmic reticulum (ER) is a continuous organelle that extends to the periphery of neurons and regulates many neuronal functions including neurite outgrowth, neurotransmission, and synaptic plasticity. Mutations in proteins that control ER shape are linked to the neurodegenerative disorder Hereditary Spastic Paraplegia (HSP). However, the ultrastructure and dynamics of the neuronal ER have been under-investigated, particularly at presynaptic terminals. Here we developed new super-resolution and live imaging methods in *D. melanogaster* larval motor neurons to investigate ER structure at presynaptic terminals from wild-type animals, and in null mutants of the HSP gene Atlastin. Previous studies indicated diffuse localization of an ER lumen marker at *Atlastin* mutant presynaptic terminals, which was attributed to ER fragmentation. By contrast, we found using an ER membrane marker that the ER in *Atlastin* mutants formed robust networks. Further, our high-resolution imaging results suggest that overexpression of luminal ER proteins in *Atlastin* mutants causes their progressive displacement to the cytosol at synapses, perhaps due to proteostatic stress and/or changes in ER membrane integrity. Remarkably, these luminal ER proteins remain correctly localized in cell bodies, axons, and other cell types such as body wall muscles, suggesting that ER tubules at synapses have unique structural and functional characteristics. This displacement phenotype has not been reported in numerous studies of Atlastin in non-neuronal cells, emphasizing the importance of conducting experiments in neurons when investigating the mechanisms leading to upper motor neuron dysfunction in HSP.

Introduction:

The endoplasmic reticulum (ER) is a continuous organelle that extends to the periphery of neurons. The ER consists of two highly dynamic structural domains known as ER sheets (which are enriched in cell bodies) and ER tubules (which are abundant in dendrites and axons) (Öztürk et al., 2020; Wu et al., 2017). The ER regulates many neuronal functions including neurite

outgrowth, neurotransmission, and synaptic plasticity (de Juan-Sanz et al., 2017; Liu et al., 2019; Oliva et al., 2020; Perez-Alvarez et al., 2020; Raffaello et al., 2016; Raiborg et al., 2015). Increasing evidence suggests that there are structural and functional differences in ER located at cell bodies, axons and presynaptic terminals. For example, the density of ER-organelle contacts varies across neuronal compartments suggesting that the functions of these contacts might be differentially regulated (Wu et al., 2017). Indeed, a recent study found that ER-endosome contacts in cell bodies exclusively regulate the size of lysosomes (Özkan et al., 2021). In addition, developing axons exhibit a unique ER ladder structure, whose function in axonal biology is still unknown (Zamponi et al., 2022). However, the cell biology and ultrastructure of these different elements of neuronal ER, particularly at presynaptic nerve terminals, have been under-investigated. This is because most studies of neuronal ER structure have either used conventional microscopy, which falls short of resolving individual ER tubules in small structures like synapses, or electron microscopy (EM), which is usually restricted to thin 2D sampling, is difficult to interpret in synaptic vesicle-rich presynaptic terminals, and does not allow examination of live dynamics (Chouhan et al., 2010; Oliva et al., 2020; Orso et al., 2009; Pérez-Moreno et al., 2023; Summerville et al., 2016; Yalçın et al., 2017; Zhu et al., 2022). Exploring the function of neuronal ER structure is important because mutations in ER-shaping genes cause neurodegenerative disorders such as Hereditary Spastic Paraplegia (HSP) and Charcot Marie Tooth Disease (Boutry et al., 2019; Fowler et al., 2019; Öztürk et al., 2020), implying that ER structure is uniquely essential for neuronal physiology.

An important ER tubule-shaping protein is Atlastin, a GTPase that regulates the homotypic fusion and tethering of ER tubules to form 3-way junctions (Lü et al., 2020). In humans, Atlastin mutations underlie one of the most common forms of autosomal dominant HSP, highlighting the importance of examining the neuron-specific functions of Atlastin in regulating ER structure (Finsterer et al., 2012). In a variety of experimental systems, *Atlastin* mutants exhibit numerous neuronal phenotypes, including defects in synaptic vesicle cycling and trafficking of neuronal cargoes (Gregorio et al., 2017), synapse development (Gregorio et al., 2017; Lee et al., 2009; Zhu et al., 2006) and axon regeneration (Rao et al., 2016). However, significant gaps remain in our understanding of how Atlastin-dependent changes in neuronal ER structure and dynamics lead to these functional defects. For example, *Drosophila Atlastin* mutants exhibit shorter ER tubule profiles in their motor neuron cell bodies by electron microscopy (Orso et al., 2009), and largely diffuse localization of an ER lumen marker in their

presynaptic terminals, which was attributed to extensive ER fragmentation. However, this fragmentation has not been validated by EM, or by fluorescence using ER membrane markers. Further, ER networks in neuronal dendrites of *C. elegans Atlastin* mutants were not fragmented but were more prone to retraction, leading to disrupted microtubule structures and mitochondria fission (Liu et al., 2019). Finally, a ladder-like ER expansion was observed in mammalian spinal axons (Zhu et al., 2022). In contrast to these neuronal findings, Atlastin knock-down in Hela or Cos-7 cells leads to long and unbranched ER tubules (Hu et al., 2009, 2015; Niu et al., 2019). Thus, loss of Atlastin leads to different ER structural phenotypes in various regions of neurons, when observed with specific reporters, and compared to non-neuronal cell types. To resolve the functions of this vital protein, comprehensive imaging studies are needed of ER organization in different regions of neurons, using complementary labeling strategies.

Another important gap exists in our understanding of neuronal ER dynamics. High-resolution imaging in non-neuronal cells has revealed transitions between ER tubules to ER sheets (Lu et al., 2009; Sun et al., 2011), ER fragmentation (Espadas et al., 2019), tubule extension and retraction (Friedman et al., 2011; Hoyer et al., 2018; Rowland et al., 2014), and alterations in 3-way junction number (Spits and Neefjes, 2021). These dynamics have been linked to various ER functions such as endosome or mitochondria fission (Friedman et al., 2011; Hoyer et al., 2018; Rowland et al., 2014) and calcium signaling (Crapart et al., 2023; Sun et al., 2011). In neurons, ER rearrangements have been suggested to alter calcium compartmentalization (Subramanian and Meyer, 1997), local protein synthesis (Deng et al., 2021; Schwarz and Blower, 2016), organelle contacts (Lu et al., 2020) and transport within the ER (Scott et al., 2021). However, the types and functions of neuronal ER dynamics, particularly in presynaptic terminals, remain largely unknown due to the challenges in imaging ER networks over time in small compartments.

New insights into the mechanisms that regulate ER structure and ER dynamics in neurons are crucial for understanding why and how mutations in ER shaping proteins, such as Atlastin, predominantly affect the nervous system. Here, we addressed this gap by examining the structure and dynamics of the ER at the *Drosophila* neuromuscular junction (NMJ) using a novel *in vivo* imaging setup and super-resolution Airyscan microscopy.

Results

100 High resolution of the ER in *Drosophila* motor neuron cell bodies, axons, and presynaptic
101 terminals
102 At presynaptic terminals of the *Drosophila* larval NMJ, the ER is highly sensitive to fixation
103 (Summerville et al., 2016) which has limited imaging experiments to live samples, often acquired
104 on upright microscopes using water dipping objectives (Chouhan et al., 2010; Oliva et al., 2020;
105 O'Sullivan et al., 2012; Pérez-Moreno et al., 2023; Summerville et al., 2016; Yalçın et al., 2017).
106 The axial resolution limit of typical water dipping objectives is >300 nm, which is insufficient to
107 distinguish the densely packed ER tubules at presynaptic terminals (Espadas et al., 2019; Wu
108 et al., 2017). To overcome this limitation, we developed a reusable imaging slide to acquire live
109 super-resolution images of neuronal ER in *Drosophila* larval fillets, using high numerical aperture
110 oil objectives and Airyscan microscopy (**Figure 1A**). Our system provides axial resolution of
111 <170 nm after processing (Del Signore et al., 2022). We imaged larval fillets using this device
112 on both inverted and upright microscopes within 40-50 min from dissection, a time frame in which
113 this preparation maintains muscle potential and the capacity for evoked neurotransmitter
114 release, even once the axon is severed from the cell body (Feng et al., 2004).
115
116 To study the live dynamics of the ER, we used Vglut-Gal4 to express either the luminal
117 ER marker BiP:sfGFP:HDEL (**Figure 1**, **2B**) or the transmembrane ER marker tdTomato:Sec61β
118 (**Figure 2A**) in *Drosophila* 3rd instar larval motor neurons. These markers were previously shown
119 to co-localize at this synapse, indicating that they are comparable reporters for visualizing
120 synaptic ER (Summerville et al., 2016). Our new imaging method allowed more precise
121 visualization of ER tubules and networks labeled by these reporters in cell bodies, axons, and
122 presynaptic terminals compared to previously reported results (**Figure 1B-D**). As previously
123 observed using lower-resolution imaging, we detected a wide variety of ER tubule structures in
124 all neuronal compartments examined (Summerville et al., 2016), including ER tubules and ER
125 sheets in cell bodies, and ER tubules in axons and presynaptic terminals. In axons, ER tubules
126 were long and we sometimes observed a ladder-like structure consisting of pairs of
127 interconnected ER tubules joined by rungs or cross-bridges, similar to structures previously
128 described in developing axons of mammalian cultured neurons (Zamponi et al., 2022) (**Figure**
129 **1C**). At presynaptic terminals, ER tubules often appeared in a highly interconnected a basket-
130 like network, while other boutons had several parallel ER tubules traversing the bouton, similar
131 to the ladder-like structures observed in axons (**Figure 1D**). Thus, we were able to detect

132 previously observed structures at approximately double the resolution previously obtained,
133 providing us with the opportunity to visualize their detailed structure and dynamics over time.
134
135 To examine the dynamics of the ER at presynaptic terminals, we collected Z stacks of
136 single boutons expressing the ER membrane marker for 40 sec at 0.65 sec/stack (**Movie S1-**
137 **S3**) or the luminal ER marker for 90 sec at 0.73 sec/stack (**Movie S4-S6**). Both markers were
138 distributed unevenly across the ER network (**Figure 2A-2B**). In particular, the luminal ER marker
139 exhibited numerous discrete round foci that moved within ER tubules with fast dynamics (<1
140 sec). Such foci were less frequently observed with the ER membrane marker (**Figure 2A-2B**,
141 **bottom**), consistent with the model that proteins in the ER lumen and ER membrane may
142 differentially cluster and move within the ER (Holcman et al., 2018; Obara et al., 2022).
143 Conversely, static regions of high intensity (which we saw for both markers) may reflect stacked
144 ER tubules (Costantini et al., 2012). We focused on the ER membrane marker to define other
145 dynamic events, since there were fewer confounding foci, and observed (1) ER budding, in which
146 a fragment of ER dissociates from the network (2) ER tubule dynamics, including overall
147 displacement of the tubule in the XY plane, as well as lengthening (extension) and shortening
148 (retraction) of the tubule (**Figure 2C-F**).
149
150 To quantify the global dynamics of the ER network in neurons expressing either the ER
151 membrane or ER lumen markers, we calculated the Pearson correlation coefficient (PCC)
152 between the 1st frame of our movies with each subsequent frame (**Figure 2G**). We observed
153 that the luminal ER marker becomes uncorrelated at a faster rate (τ = 37.08s) than the ER
154 membrane marker ($\tau = 61.82$s), suggesting more rapid changes in ER dynamics. We
155 hypothesize the differences in the dynamics of the luminal and membrane markers are due to
156 the highly mobile nature of luminal ER marker foci within the ER network (**Figure 2B**). However,
157 despite these differences, the correlation coefficients for both ER markers were still relatively
158 high throughout the imaging period: The first and last frames of the luminal ER marker had a
159 PCC of 0.74 and the membrane ER marker had a slightly higher PCC of 0.85. Thus, the overall
160 structure of the ER network changes only modestly during the time-course of our movies
161 suggesting it is relatively stable in these neurons, which are at rest (**Figure 2A**). We also
162 qualitatively categorized synaptic boutons as “dynamic” or “non-dynamic”. We categorized a
163 bouton as dynamic if we observed any changes in the structure of the ER network such as ER
164 tubule movement and foci dynamics. We found that 86% of boutons were dynamic while 14%

165 were not dynamic (**Figure 2D**). Overall, these results show that we can capture live ER dynamics
166 at high resolution in *Drosophila* motor neurons.
167
168 <u>*Atlastin* mutant synapses have robust ER networks but reduced levels of ER membrane markers</u>
169
170 We first aimed to correlate ER structure with neuronal development and function to
171 interrogate the potential physiological functions of presynaptic ER structure and dynamics. To
172 this end, we examined a mutant of the ER-shaping protein, Atlastin. Mammals have three
173 Atlastin homologs and Atlastin-1 is enriched in the brain, while *Drosophila* has a single Atlastin
174 homolog (Rismanchi et al., 2008). As in previous studies of *Atlastin* mutant phenotypes in
175 *Drosophila*, we used transheterozygotes of the *Atlastin* null mutant atl^2 and a 3rd chromosome
176 deficiency (def) removing the *Atlastin* locus, to eliminate confounding effects from second site
177 mutations (Lee et al., 2009). Most atl^2/atl def mutants (from now on termed *Atlastin* mutants)
178 were pharate lethal with few escapers, and we observed that 3rd instar larval presynaptic
179 terminals had a significant increase in satellite boutons (**Figure 3 Supplement A**), indicating
180 defects in synaptic growth and development, as previously reported (Gregorio et al., 2017; Lee
181 et al., 2009).
182
183 First, we used Airyscan microscopy to examine ER network structures at *Atlastin* mutant
184 presynaptic terminals expressing the ER membrane marker tdTomato:Sec61β. A previous study
185 used confocal microscopy of the ER lumen marker BiP:sfGFP:HDEL to examine ER structure in
186 *Drosophila Atlastin* mutant presynaptic terminals, and observed a highly diffuse distribution of
187 the marker, which was attributed to extensive ER fragmentation (Summerville et al., 2016). We
188 reasoned we would observe a similar phenotype in *Atlastin* mutants expressing an ER
189 membrane marker. However, *Atlastin* mutants expressing the ER membrane marker did not
190 exhibit diffuse or fragmented signal, and had tubular ER networks that were qualitatively similar
191 to controls (**Figure 3A-B**). We observed no significant difference in the density of complex
192 basket-like structures or simple basket-like structures labeled with tdTomato:Sec61β, despite
193 the smaller size of satellite boutons in *Atlastin* mutants (**Figure 3C-D**). Our results suggest that
194 there are indeed ER networks in *Atlastin* mutant synapses (rather than extensive fragmentation)
195 and that structural defects underlying the previously observed loss of synaptic functions are likely
196 specific to a subset of ER structural or dynamic properties. Further, our findings show that

197 luminal and membrane ER markers have distinct phenotypes in *Atlastin* mutants, which we
198 investigate further below (see **Figures 4-7)**.
199
200 To further explore ER architecture in the *Atlastin* mutant we generated masks of ER from
201 boutons with complex basket-like structures (**Figure 3E**). We found a small but significant
202 increase in the fraction of bouton area occupied by ER in *Atlastin* mutants compared to controls
203 (**Figure 3F**), suggesting that their architectures are subtly different. We also found that the
204 marker tdTomato:Sec61β exhibited lower fluorescence levels in *Atlastin* mutant boutons, as
205 quantified by its mean intensity within the segmented ER area in live preparations (**Figure 3G**),
206 as well as over the entire presynaptic terminal in fixed preparations (**Figure 3 Supplement – B-**
207 **D**). This reduction in ER membrane marker intensity has also been observed in other HSP
208 mutants, suggesting this is a common feature of ER shaping mutants, and could indicate
209 changes in ER membrane composition or integrity (Pérez-Moreno et al., 2023). Finally, we noted
210 that the Coefficient of Variation (CoV) of tdTomato:Sec61β signal was significantly higher in
211 *Atlastin* mutants (**Figure 3 Supplement E**), suggesting that it is more concentrated in
212 subsynaptic structures compared to wild-type synapses (notably the opposite of what would be
213 expected for fragmentation). Overall, our data suggests ER networks exist in *Atlastin* mutant
214 synapses, distinct from the diffuse distribution seen with a luminal ER marker, and that they may
215 have quantitative differences in architecture compared to wild-type synapses.
216
217 <u>Presynaptic terminals of *Atlastin* mutants are sensitized to the overexpression of a luminal ER</u>
218 <u>marker</u>
219 Our ER membrane marker results are in sharp contrast to a previous study examining the
220 ER structure of *Atlastin* mutants with the luminal ER marker, BiP:sfGFP:HDEL. This study
221 concluded from the diffuse distribution of this marker at synapses that the ER was highly
222 fragmented in *Atlastin* mutants (Summerville et al., 2016). Since we did not observe
223 fragmentation with the ER membrane marker, we used Airyscan microscopy to re-examine the
224 luminal ER marker BiP:sfGFP:HDEL in *Atlastin* mutants. Unlike its strict localization to the ER
225 network in control synapses, we reproduced the observation that a large fraction of
226 BiP:sfGFP:HDEL was diffusely localized in *Atlastin* mutant synapses, even at the resolution of
227 Airyscan microscopy. Further, the marker extended to the boundary of presynaptic terminals,
228 suggesting that it may be mislocalized to the cytosol (**Figure 4A-B**). We identified two distinct
229 ER structure phenotypes in *Atlastin* mutants: NMJs with “Phenotype A” had diffuse

230 BiP:sfGFP:HDEL but also had an identifiable ER network structure, while NMJs with “Phenotype
231 B” had a more severe phenotype with no visible ER network structures. We blinded our images
232 and categorized control and *Atlastin* mutant datasets as “Phenotype A”, “Phenotype B” or no
233 phenotype (**Figure 4C**). In *Atlastin* mutants, we found that 45% of NMJs exhibited “Phenotype
234 A”, 55% of NMJs exhibited “Phenotype B” and 10% of the NMJs had no phenotype. We observed
235 Phenotypes A and B in both anterior (segment A2) and posterior (segment A5) muscle
236 segments, in Is (phasic) and Ib (tonic) motor neuron subtypes, and in neurons innervating
237 multiple different body wall muscles, suggesting that it reflects a widespread phenomenon in
238 motor neuron synapses of *Atlastin* mutants (**Figure 4 - Figure Supplement 1**). Interestingly, we
239 observed a shift in the distribution of presynaptic terminals with Phenotype B in *Atlastin* mutants
240 towards lower mean intensities of the marker (**Figure 4D**). This could suggest that the luminal
241 ER marker is either degraded or removed from presynaptic terminals, leading to lower levels.
242 We also observed a significant change in its coefficient of variance (CoV) due to redistribution
243 of the luminal ER marker in *Atlastin* mutants (**Figure 4F**). Together with our finding that a
244 membrane-associated ER marker does not show fragmentation but exhibits lower intensity,
245 these results raise the possibility that the luminal ER marker is mislocalized to the cytosol and
246 that there may be changes to the structural integrity of the ER membrane. We were unable to
247 assess co-localization of BiP:sfGFP:HDEL and tdTomato:Sec61β, as very few larvae co-
248 expressing these markers survived, and the few that did exhibit grossly defective NMJ
249 morphology and large aggregates of both markers. Further, adult flies expressing
250 BiP:sfGFP:HDEL were unhealthy and could not be maintained as a stock, suggesting that this
251 marker is toxic even in otherwise wild-type flies. Taken together, these results suggest that
252 *Atlastin* mutants are particularly sensitized to overexpression of the BiP:sfGFP:HDEL marker.
253
254 To ask if the luminal ER marker displacement phenotype is specific to neurons or
255 presynaptic terminals, we examined the ER in body wall muscles of *Atlastin* mutants and did not
256 observe the luminal ER marker displaced to the cytosol (though we noticed reduced network
257 complexity, as previously reported (Lee et al., 2009) (**Figure 5, right**). Next, we examined the
258 cell body and axons of *Atlastin* mutants to determine if the displacement of the luminal ER marker
259 was a global or local phenotype within neurons. As previously reported (Summerville et al.,
260 2016), we did not observe a diffuse signal for the luminal ER marker in cell bodies or axons
261 (even within ~30μm of the synapse) (**Fig 5, middle**). However, we did observe ER fragmentation

262 in some axons (**Fig 5, left**). These results indicate that the sensitivity of *Atlastin* mutants to
263 BiP:sfGFP:HDEL reflects a synapse-specific function.
264
265
266 The luminal ER phenotype in *Atlastin* mutants is progressive
267
268 Atlastin disruption is linked to the neurodegenerative disorder HSP, which is a progressive
269 disease in which patients lose neuronal function over time (Blackstone, 2018, 2012; Blackstone
270 et al., 2011). Indeed, *Drosophila Atlastin* mutants recapitulate progressive motor dysfunction as
271 observed in HSP patients (Gregorio et al., 2017). To test the hypothesis that Phenotype A might
272 similarly progress to Phenotype B, we examined 1st instar larvae and categorized control and
273 *Atlastin* mutant datasets as described above. If the phenotype is progressive, we predicted that
274 we would observe a lower fraction of NMJs with diffuse luminal ER marker and an increase in
275 the fraction of synapses with no phenotype. Indeed, we observed a decrease to 12.5% of NMJs
276 with Phenotype B in 1st instar compared to 55% in 3rd instar, and an increase to 38% of NMJs
277 with no phenotype in 1st instar compared to 10% in 3rd instar (compare **Figure 4A-C** to **Figure**
278 **6**). These results suggest that displacement of the luminal ER marker progresses over time and
279 that this phenotype is initiated early in neuronal development.
280
281 Luminal proteins are likely located in the cytosol in *Atlastin* mutants
282
283 Our results show diffuse BiP:sfGFP:HDEL in *Atlastin* mutants (even at high resolution)
284 compared to robust ER networks marked by tdTomato:Sec61β. This suggests that the luminal
285 marker is not in small ER membrane fragments as previously concluded, and instead may be
286 displaced to the cytosol without being associated with ER membranes. To test this hypothesis,
287 we treated presynaptic terminals for 5 min with the mild detergent digitonin to gently permeabilize
288 the plasma membrane and extract proteins from the cytosol (**Figure 7A**). We hypothesized the
289 digitonin treatment would lead to loss of fluorescence in *Atlastin* mutants, proportional to the
290 fraction of the luminal ER marker protein in the cytosol (**Figure 7B**). We imaged the same
291 presynaptic terminal (expressing either cytosolic GFP or BiP:sfGFP:HDEL) both before and after
292 digitonin treatment. To identify presynaptic terminals, we also labeled our live samples with α-
293 HRP antibodies (Snow et al., 1987).
294

295 We measured the fraction change in mean intensity to determine the effects of digitonin
296 treatment on cytosolic and ER markers (**Figure 7C**). For cytosolic GFP, we observed a
297 significant loss in mean fluorescence in all our samples (13/13) following digitonin treatment.
298 Control presynaptic terminals expressing the luminal ER marker, BiP:sfGFP:HDEL, became
299 highly fragmented following digitonin treatment, perhaps due to changes in the osmolarity of the
300 cytosol, which has been previously shown to promote ER fragmentation (King et al., 2020).
301 However, most of this fragmented ER did not escape the synaptic terminal, indicating that ER
302 fragments were not extracted or severely permeabilized with this treatment. Interestingly, in half
303 the control samples (9/18) the marker redistributed to bright puncta and showed an unexpected
304 increase in mean intensity. Digitonin treatment may allow the exchange of small molecules into
305 the ER (Le Gall et al., 2004), perhaps changing the fluorescent properties of sfGFP. The other
306 half of samples (9/18) had slightly reduced mean intensity following digitonin treatment, possibly
307 due to moderate loss of ER fragments. Next, we categorized and analyzed *Atlastin* mutants with
308 Phenotype A or Phenotype B. In *Atlastin* mutants with Phenotype A, we observed no significant
309 difference from controls following digitonin treatment. We observed that half (5/10) of our
310 samples increased their mean intensity levels following digitonin treatment while the other half
311 had a decrease (5/10). We also observed that *Atlastin* mutant synapses exhibiting Phenotype A
312 had puncta following digitonin treatment similar to control (likely because Phenotype A terminals
313 have some ER network visible with the luminal marker). In contrast, we observe a decrease in
314 fluorescence intensity following digitonin treatment in most (8/10) *Atlastin* mutant presynaptic
315 terminals with Phenotype B (which have almost no visible ER networks with the luminal marker).
316 These data suggest that the population of luminal ER molecules sensitive to digitonin in *Atlastin*
317 mutants is likely displaced to the cytosol (though we cannot rule out very small ER fragments).
318

319 **Discussion**

320

321 We introduce in this study an innovative *in vivo* imaging system to study the architecture
322 and dynamic behaviors of *Drosophila* neuronal ER networks. Our imaging system is versatile
323 and can be used to visualize genetically encoded fluorescent proteins in diverse larval tissues.
324 For the first time, we examined and defined the dynamic properties of ER networks at
325 presynaptic terminals *in vivo*, providing a foundation for future studies to identify the function of
326 the various ER structural rearrangements observed at presynaptic terminals. Using our high-
327 resolution system, we found that *Atlastin* mutant presynaptic terminals are sensitive to

328 overexpression of a luminal ER marker, likely resulting in its displacement to the cytosol.
329 However, they form robust networks with only subtle defects when labeled by an ER membrane
330 marker. Our results show that Atlastin plays unique and synapse-specific roles in regulating the
331 structure and function of ER, which may underlie its numerous previously reported deficits in
332 synaptic function.
333
334 **ER network dynamics at presynaptic terminals**
335
336 We categorized ER dynamics at presynaptic terminals as: (1) Budding and fusion of
337 vesicular structures, (2) ER tubule dynamics, and (3) dynamics of foci that are retained within
338 the ER network. Future work is needed to directly examine the function of these dynamics at
339 presynaptic terminals, but we speculate below on their potential functions. Neurons are highly
340 polarized cells and membrane trafficking pathways can have specialized functions at presynaptic
341 terminals (Deshpande and Rodal, 2016). ER-derived vesicles could act as localized calcium
342 signaling hubs (Burgoyne et al., 2015) or serve as sites for compartmentalized local translation
343 if they carry ribosomes (Carter et al., 2020; Deng et al., 2021). Other pathways involving the
344 formation of ER vesicles include ER-to-Golgi transport and ER autophagy (ER-phagy) (Chino
345 and Mizushima, 2020). However, the synaptic ER vesicle-like structures that we observed are
346 unlikely to be involved in the secretory pathway or ER-phagy because these vesicles re-fuse
347 with the ER. Second, ER tubule dynamics play multiple roles, such as maintaining the tension
348 of the ER network (Espadas et al., 2019; Niu et al., 2019) and forming ER-organelle contacts
349 (Friedman et al., 2011; Hoyer et al., 2018; Rowland et al., 2014). ER contacts occur at the tips
350 and edges of ER tubules, and they have diverse functions, such as promoting mitochondria and
351 endosome fission (Friedman et al., 2011; Hoyer et al., 2018; Rowland et al., 2014). Future
352 studies should perform co-localization experiments with these other organelles or generate ER-
353 organelle sensors to determine if ER tubule dynamics are important for these functions at
354 presynaptic terminals. The last type of ER dynamics we identified is focus dynamics within ER
355 networks. We hypothesize that foci emerge due to changes in the dynamics of protein clusters
356 at the ER membrane or within the lumen. Foci dynamics occur at higher levels with the luminal
357 ER marker in contrast to those observed with the ER membrane marker. This suggests that
358 proteins in the lumen are not evenly distributed compared to proteins at the ER membrane. Our
359 work provides a framework to shed light on the unique features of the structure and dynamics of
360 the presynaptic ER.

361

362 **Presynaptic ER network structures are only modestly perturbed in *Atlastin* mutants but**
363 **are sensitized to overexpression of luminal proteins**

364

365 Using the membrane marker tdTomato:Sec61β, we discovered that *Atlastin* mutants do
366 indeed have ER networks at presynaptic terminals. This is in sharp contrast to the diffuse
367 distribution that we and others observe for the lumenal marker BiP:sfGFP:HDEL, and argues
368 against excessive ER fragmentation in these mutants (since we would in that case expect to
369 also see fragmented membranes). While we did not observe gross defects in ER network
370 structure using the membrane marker, our quantitative analysis revealed subtle differences in
371 the overall distribution of tubules as well as of Sec61β itself. Future analyses of dynamics at
372 Atlastin mutant synapses may reveal additional insights into how this ER shaping protein
373 controls synaptic transmission, signaling, and development.

374

375 Given the very different phenotypes observed with each marker, which more accurately
376 reflects the *Atlastin* mutant phenotype in the absence of any ER marker? We favor the
377 hypothesis that the true *Atlastin* ER phenotype is more likely to be similar to the
378 tdTomato:Sec61β distribution, and that BiP:sfGFP:HDEL overexpression further disrupts the ER
379 in *Atlastin* mutants, for the following reasons: (1) tdTomato:Sec61β-expressing animals still show
380 Atlastin-associated functional defects such as defective synaptic growth, indicating that Atlastin-
381 dependent ER functions are disrupted without dramatic defects in ER structure; (2)
382 BiP:sfGFP:HDEL exhibits some toxicity even in wild-type adult animals. (3) The
383 BiP:sfGFP:HDEL phenotype becomes more severe over larval development, suggesting that it
384 is a progressive gain-of-function. Our study underscores the need to generate new endogenous
385 ER markers in *Drosophila* to minimize the detrimental effects of protein overexpression of ER
386 lumen or ER membrane markers. Future studies should also examine ER mutants with both ER
387 membrane and ER lumen markers, as specific defects could affect one and not the other, as
388 observed in *Atlastin* mutants.

389

390 Why then might *Atlastin* mutants displace luminal proteins to the cytosol upon
391 overexpression of the BiP:sfGFP:HDEL? Several possibilities include reduced ER membrane
392 integrity, activation of ER-associated protein degradation (ERAD), disruption of protein
393 translocation, or induction of ER stress permeability. We outline below how these pathways

394 could contribute to the displacement phenotype in *Atlastin* mutants. First, *Atlastin* mutants have
395 lower levels of the ER membrane marker Sec61β and altered ER network structures that could
396 indicate changes in the integrity of the ER membrane. ER tubules at presynaptic terminals of
397 *Atlastin* mutants could therefore be susceptible to rupture when luminal proteins are
398 overexpressed, resulting in passive displacement to the cytosol. Second, luminal proteins in
399 *Atlastin* mutants could be targeted for extrusion from the ER through ERAD (Christianson et al.,
400 2023). However, this seems unlikely since these proteins would be targeted for degradation by
401 the proteasome in the cytosol, and we still observe luminal proteins in presynaptic terminals of
402 *Atlastin* mutants. Third, protein translocation defects could promote the accumulation of luminal
403 proteins in the cytosol (McKibbin et al., 2012). However, defective protein translocation would
404 likely result in a global displacement of luminal proteins, especially in the cell body, which is the
405 primary site of neuronal protein translation (Glock et al., 2021). Instead, the diffuse phenotype
406 is specific to presynaptic terminals. However, our observation that *Atlastin* mutants have reduced
407 levels of the ER membrane marker Sec61β could reflect mild translocation defects.
408 Nevertheless, this defect is not likely to result in total displacement of luminal ER proteins at
409 presynaptic terminals of *Atlastin* mutants with Phenotype B. Fourth, ER stress induced by
410 apoptosis can increase the permeability of the ER membrane (without bursting), enabling luminal
411 ER proteins to diffuse to the cytosol (Wang et al., 2011). However, we did not find the neuronal
412 debris that is commonly observed at muscles following neuronal apoptosis, in either first or third-
413 instar larvae of *Atlastin* mutants (Aponte-Santiago et al., 2020; Graf et al., 2011).
414
415 Finally, it is important to note that we found that only presynaptic terminals of *Atlastin*
416 mutants are susceptible to the over expression of the BiP:sfGFP:HDEL marker, indicating unique
417 properties of synaptic ER compared to other neuronal compartments. Previously, a ladder-like
418 ER expansion was observed in mammalian spinal axons of Atlastin-fusion incompetent mutants,
419 providing another example of spatially distinct Atlastin-dependent ER network structures (Zhu et
420 al., 2022). We observed similar ladder-like structures in both control and *Atlastin* mutant axons
421 labeled with tdTomato:Sec61β. Interestingly, the presence of a ladder-like structure and baskets
422 at synapses argues against the notion that Atlastin is the sole protein responsible for shaping
423 ER tubule fusion in axons. This is in contrast to the long and unbranched ER tubules found in
424 Atlastin-deficient Hela or Cos-7 cells (Hu et al., 2009; Niu et al., 2019), and suggests that
425 compensatory tubule-fusion machinery might be specific to neurons. This discrepancy warrants
426 further investigation to gain a clearer understanding of the underlying mechanisms at play. We

427 also found that *Atlastin* mutants have reduced Sec61β levels at the ER membrane of presynaptic
428 terminals. This decrease in Sec61β parallels findings in *Drosophila* mutants of Reticulon 1,
429 another ER shaping and HSP linked gene. This study found that in addition to Sec61β, other ER
430 membrane proteins, such as STIM and Stukorf, exhibited lower levels on ER tubules, suggesting
431 overall changes in the levels of proteins at the ER membrane (Pérez-Moreno et al., 2023).
432 However, unlike *Atlastin* mutants, Reticulon 1 mutants are not sensitized to the overexpression
433 of luminal proteins (Pérez-Moreno et al., 2023). This suggests that ER networks of *Atlastin*
434 mutants have unique features compared to those of other ER-shaping proteins. Future work
435 should comprehensively examine the common and unique defects associated with Atlastin
436 dysfunction across neuronal compartments.
437
438 **Methods**
439
440 *Drosophila* stocks
441 *Drosophila melanogaster* was cultured on a standard medium at 22–25°C. Detailed genotypes
442 and sexes used for experiments are described in Table S1. Stocks used in this study
443 include: Vglut-Gal4 (Bloomington *Drosophila* Stock Center (BDSC #: 24635), BG57-Gal4 (gift
444 from Vivian Budnik), atl^2 (gift from James McNew), third chromosome deficiency (BDSC #:
445 7948), UAS-BiP:sfGFP:HDEL (BDSC #: 24635), 20XUAS-tdTomato:Sec61β (BDSC #: 64746),
446 UAS-CD8:RFP (BDSC #: 27391) and UAS-GFP (gift from Griffith lab).
447
448 Live imaging of luminal and membrane ER markers
449 1st and wandering 3rd instar larvae were dissected in Ca^{2+}-free HL3.1 (Feng et al., 2004) and
450 axons were severed from the central nervous system. Dissections were performed in the live
451 imaging slide described below. Larvae were imaged at room temperature with a 63X (n.a. 1.4)
452 oil immersion objective, using an Airyscan LSM 880 microscope in super-resolution mode and
453 Zen Black software. Raw image stacks were processed in Zen Blue or Zen Black using 3D
454 Airyscan processing with automatic settings.
455
456 For 3rd instar larvae, Z-stacks of presynaptic type Ib terminals at muscle 4 in segment A5 (unless
457 otherwise noted) were acquired to measure the levels of luminal ER markers, to categorize ER
458 network phenotypes, or for morphological measurements. For 1st instar larvae, live larval fillets
459 were stained with 1/250 1.5 mg/ml HRP Alexa Fluor 647 (Jackson ImmunoResearch) in HL3.1

460 for 5 min followed by a 1 min wash. Next, Z-stacks of 1st instar presynaptic terminals at muscle
461 4 in segment A3-A5 were acquired and used to categorize ER network phenotypes.
462
463 To record the dynamics of the luminal ER marker BiP:sfGFP:HDEL, Z-stacks of a single bouton
464 (8 slices with 0.5 micron spacing) were collected for 100 frames at a frame rate of 0.73
465 seconds/stack. To record ER dynamics with the membrane ER marker tdTomato:Sec6β, Z-
466 stacks of a single bouton (8 slices with 0.5 micron spacing) were collected for 60 frames at a
467 frame rate of 0.65 seconds/stack. Imaging for longer periods led to significant photobleaching.
468
469 Construction of *in vivo* imaging slide for *Drosophila* larvae
470 To make the reusable imaging slide, Press-To-Seal Silicone Isolators (Grace Bio-labs; CQS-
471 13R-2.0) were mounted onto rectangular glass slides, which then were filled from their centers
472 to their tops with Krayden Dow Sylgard 184 Silicone (Thermo Fisher Scientific). Each slide with
473 a Press-To-Seal Silicone Isolator was leveled to ensure the silicone cured evenly at room
474 temperature. Minutien pins (Fine Science Tools) were cut with nail clippers and used to stretch
475 the larvae and fix it in place. Pins were pressed into the cured Sylgard 184 Silicone and a few
476 drops of hemolymph-like solution HL3.1 were added. Next, a coverslip was placed on top of the
477 dissected larvae, each corner was gently pressed down, and excess HL3.1 was removed with a
478 Kimwipe, thus sealing the coverslip to the silicone isolator.
479
480 Fixed tissue staining
481 Wandering 3rd instar larvae were dissected in Ca^{2+}-free HL3.1 and fixed for 17 min in Ca^{2+}-free
482 HL3.1 containing 4% PFA. Larvae were blocked and permeabilized overnight in PBS containing
483 0.25% Saponin, 2.5% normal goat serum (NGS), 2.5% bovine serum albumin (BSA), and 0.1%
484 sodium azide. Fixed larvae (**Figure 3 - Supplement**) were stained with 1/500 FluoTag®-X4 anti-
485 RFP (#N0404, Nanotag Biotechnologies) at 4°C for 24 hrs and with 1/100 HRP Alexa Fluor 647
486 at room temperature for 2hrs. Stained larvae were mounted in ProLong Diamond Antifade
487 Mountant (#P36970; Thermo-Fisher Scientific, Waltham, MA, USA). Z-stacks were collected of
488 *Drosophila* larval NMJs in muscle 4 of segment A5 with a spinning disk confocal microscope at
489 room temperature on a Nikon Ni-E upright microscope equipped with 100x (n.a. 1.45) oil
490 immersion objective, a Yokogawa CSU-W1 spinning-disk head, an Andor iXon 897U EMCCD
491 camera. Images were collected using Nikon Elements AR software.
492

493 Digitonin experiments

494 Digitonin experiments were conducted in live fillets from larvae expressing the luminal ER
495 marker, UAS-BiP:sfGFP:HDEL under the control of the neuronal driver Vglut-GAL4. Fillets were
496 stained with 1/500 1.5 mg/ml HRP Alexa Fluor 594 (Jackson ImmunoResearch) or 1/250 HRP
497 Alexa Fluor 647 in HL3.1 for 5 min, followed by a 1 min HL3.1 wash. Next, pre-digitonin Z-stacks
498 were acquired from muscle 4 NMJs from segments A3 to A5 (both hemisegments) using the
499 spinning disk confocal microscope described above. Fillets were subsequently incubated with
500 0.05% digitonin in HL3.1 for 5 min, then rinsed with HL3.1 and re-incubated with HRP Alexa
501 Fluor 594 or HRP Alexa Fluor 647 for 5 min. Preps were then washed for 1 min with HL3.1.
502 Finally, post-digitonin Z-stacks were acquired of the same NMJs.

503

504 Image analysis

505 Debris, axons, and large fluorescent aggregates (sometimes observed for tdTomato:Sec61β)
506 were manually removed from all images before analyses of maximum projections or Z-stacks.
507 Neuronal masks were created by first conducting a background subtraction of the image (rolling
508 ball, 50 pixel radius), and then introducing a gaussian blur before thresholding using Otsu or Li
509 algorithms. For live image analysis, maximum intensity projections of each timepoint were
510 corrected for (1) photobleaching using histogram matching and (2) sample drift or muscle
511 contraction using the StackReg plugin (Thevenaz et al., 1998).

512

513 *Pearson correlation coefficient (PCC) for measurement of ER dynamics:* To measure the PCC
514 of ER membrane or luminal proteins, we employed a FIJI macro consisting of the following steps:
515 (1) We created an NMJ mask of the neuronal outline of presynaptic terminals using the ER
516 membrane or luminal ER protein marker. (2) We measured the PCC between the 1st frame of
517 the movie and every other frame. (3) We plotted the PCC over time to measure global changes
518 in ER structure.

519

520 *Segmentation of presynaptic ER networks (**Figure 3C-E**):* For segmentation, time-lapse movies
521 of boutons with complex basket-like ER networks were selected from control and *Atlastin*
522 mutants. Images were blinded and maximum projections were created to segment the ER in
523 FIJI. We used the Trainable Weka Segmentation (TWS) machine-learning tool (Arganda-
524 Carreras et al., 2017) to manually annotate the first and last time-points in each movie as a
525 training dataset, and generated a mask of the ER throughout the movie. The mask from the first

526 time-point was then used for analysis. Bouton masks were created by background subtraction
527 and blurring of the tdTomato:Sec61β signal to quantify the fraction ER area. Finally, the mean
528 intensity of the ER membrane marker tdTomato:Sec61β was calculated within the ER mask.
529
530 *Presynaptic levels of ER membrane* marker tdTomato:Sec61β *(**Figure 3 Supplement**)*: *A*
531 custom FIJI macro consisting of the following steps was employed on maximum intensity
532 projections,: (1) An NMJ mask was created using the α-HRP neuronal marker; (2) The integrated
533 density of the ER membrane marker tdTomato:Sec61β was measured within the α-HRP mask;
534 (3) The mean intensity of the ER membrane marker at presynaptic terminals was calculated by
535 dividing the tdTomato:Sec61β integrated density by the area of the presynaptic terminal.
536
537 *Analysis of NMJ morphology:* Satellite and total bouton number were manually counted from
538 blinded maximum intensity projections of fixed and α-HRP labeled larvae. Satellite boutons were
539 defined as any string of 5 or fewer boutons extending from the main axis of the NMJ.
540
541 *Categorization of ER morphology and dynamics:* For analysis of tdTomato:Sec61β–labeled ER
542 structures (**Figure 3C-G)**, maximum intensity projection images were blinded and the following
543 structures were categorized: (1) Complex baskets had three or more crossing ER tubules; (2)
544 Simple baskets formed a single circle of ER tubules, often close to the periphery of the bouton.
545 The number of such structures was then normalized to the length of the NMJ arbor in the image
546 (excluding any arbor under 50 μm), which was measured by manually tracing and summing the
547 lengths of each branch of the NMJ.
548
549 For dynamics analysis (**Figure 2**), we used the same dataset as the control in **Figure 3E-G.**
550 Boutons with complex basket-like ER networks were selected for analysis. Maximum intensity
551 projection timelapse movies were blinded and replayed 3-4 times before categorization. We
552 identified three distinct categories of ER dynamics in presynaptic terminals of *Drosophila* motor
553 neurons (note that a single bouton can exhibit multiple types of dynamics): (1) **ER budding** –
554 small vesicle-like structures emerging from the ER network and re-fusing in a different region;
555 (2) **ER tubule dynamics**, encompassing four subcategories as follows: (a) Tubule
556 displacement, involving tubules that changed their localization within boutons without detaching
557 from the ER network; (b) Tubule extension, where an ER tubule emerged and extended from

558 the ER network; (c) Tubule retraction, characterized by the retraction and disappearance of an
559 ER tubule from the ER network; and (d) Tubule extension and retraction, indicating an ER tubule
560 both extending and retracting from the ER network within the timelapse. (3) **Foci dynamics** –
561 round, bright puncta moving within the ER network and (4) **no dynamics** – boutons that lacked
562 observable dynamics.
563
564 *Presynaptic levels of luminal ER proteins at Drosophila motor neurons:* A custom FIJI macro
565 consisting of the following steps was employed on Z-stacks: (1) We created an NMJ mask using
566 the luminal ER protein marker. (2) Using this mask, we measured the neuron volume and the
567 integrated density of the marker. (3) We calculated the mean intensity of the marker by dividing
568 the integrated density by the volume of the presynaptic terminal.
569
570 *Categorization of luminal ER marker distribution:* Images were blinded before analysis to ensure
571 unbiased qualitative analysis of luminal ER marker BiP:sfGFP:HDEL in controls and *Atlastin*
572 mutants. Maximum intensity projections were then sorted into three phenotypic categories: (1)
573 **"Phenotype A"** - luminal ER marker localizes to ER networks but is partially displaced to the
574 cytosol, (2) **"Phenotype B"** - luminal ER marker mostly displaced to the cytosol and ER
575 networks are not detectable, and (3) **"No phenotype"** - luminal ER marker completely localizes
576 to ER networks.
577
578 *Presynaptic levels of cytosolic or luminal ER proteins pre- and post-digitonin treatment*: Images
579 were blinded and maximum projections were created for further analysis. Neuronal outlines were
580 obtained by manually tracing the α-HRP-positive region in FIJI. Next, the integrated density of
581 UAS-GFP or UAS-BiP:sfGFP:HDEL was quantified within the manually traced neuronal outlines.
582 Mean intensity was calculated by dividing the integrated density by the area of the presynaptic
583 terminal.
584
585 Statistics
586 GraphPad Prism software was used to perform statistical analyses and generate graphs.
587 Statistical analyses were conducted using parametric tests (e.g. one-way ANOVA, Student's t-
588 test) for normally distributed data, and non-parametric tests (e.g. Kruskal-Wallis, Mann-Whitney
589 tests) if the data was not normally distributed. Chi-squared tests were used for categorical data.
590 p-values were set to *<0.05, **<0.01, ***<0.001.

591

592 **Acknowledgements:**

593

594 We thank the Bloomington *Drosophila* Stock Center (Indiana University, Bloomington, IN, NIH
595 P40OD018537) and James McNew for fly lines, and Steve Del Signore for help with image
596 analysis. This work was supported by NINDS grants R01 NS103967 to A.A.R. and T32 007292
597 to M.C.Q.-F.

598

599 **Figure legends:**

600

601 **Figure 1. *In vivo* imaging of ER networks in *Drosophila* motor neurons.** (**A**) Schematic of
602 setup for live imaging experiments in this study, consisting of a glass slide with a mounted
603 silicone isolator filled with Sylgard. Small metal pins were used to stretch the larvae (small round
604 dots). Finally, a coverslip was placed on top of the larval fillet for imaging with an oil objective on
605 upright or inverted microscopes. (**B**) A representative single slice of an Airyscan microscopy Z-
606 stack of the center (top) or periphery (bottom) of the cell body of a motor neuron expressing the
607 luminal ER marker BiP:sfGFP:HDEL. Arrows indicate ER tubules and sheets. (**C**) Maximum
608 projections of Z-stacks acquired with an Airyscan microscope of two different motor neuron
609 axons expressing the luminal ER marker BiP:sfGFP:HDEL. (**D**) Representative maximum
610 projection of a Z-stack acquired with an Airyscan microscope of a motor neuron presynaptic
611 terminal expressing the luminal ER marker BiP:sfGFP:HDEL. The magenta outline highlights the
612 neuronal boundary. Arrows indicate boutons containing ER baskets or ladder-like ER structures.

613

614 **Figure 2. Dynamics of luminal and membrane ER markers at presynaptic terminals.** (**A**,
615 **top**) Maximum intensity projection of Airyscan Z-stacks from the beginning (t=0) and the end
616 (t=39 sec) of a timelapse movie (**Movie S1**) of a single wild-type bouton expressing the ER
617 membrane marker tdTomato:Sec61β. (**A, bottom**) Magnification of the region in the dotted red
618 box of dynamics observed from 0 sec to 1.4 sec of the movie. (**B, top**) Maximum intensity
619 projection of Airyscan Z-stacks from the beginning (t=0) and the end (t=72 sec) of a timelapse
620 movie (**Movie S4**) of a single wild-type bouton expressing the luminal ER marker
621 BiP:sfGFP:HDEL. (**B, bottom**) Magnification of the region in the dotted red box of dynamics
622 observed from 0 sec to 1.4 sec of the movie. (**C**) Presynaptic terminals exhibiting ER budding,
623 focus dynamics and various types of ER tubule dynamics (ER tubule displacement, tubule

624 extension, and tubule retraction). (**D**) Qualitative categorization of the percentage of boutons
625 that are dynamic or not dynamic expressing the ER membrane marker tdTomato: Sec61β. (**E**)
626 Qualitative categorization of the percentage of dynamic boutons expressing the ER membrane
627 marker tdTomato: Sec61β that exhibit ER budding, foci dynamics or ER tubule dynamics. (**F**)
628 Qualitative categorization of the percentage of dynamic boutons expressing the ER membrane
629 marker tdTomato: Sec61β that exhibit tubule displacement, tubule extension, tubule retraction
630 and both tubule extension and retraction. (**G**) Pearson's Correlation Coefficient (PCC) of the first
631 frame (t0) with each subsequent frame (tn) in movies of boutons expressing the ER membrane
632 marker tdTomato: Sec61β (gray, n = 14 boutons) or ER luminal marker BiP:sfGFP:HDEL (green,
633 n = 10 boutons). The shaded area shows the standard deviation, and the solid black line
634 indicates the mean. The table shows the results of a non-linear fit of each marker's dataset.
635
636 **Figure 3. *Atlastin* mutants expressing the ER membrane tdTomato:Sec61β exhibit robust**
637 **ER networks.** (**A, B**) Representative maximum projection of a Z-stack acquired live by Airyscan
638 microscopy of control and *Atlastin* mutant NMJs expressing the ER membrane marker tdTomato:
639 Sec61β at presynaptic terminals. These images are not contrast matched because *Atlastin*
640 mutants exhibit lower levels of the tdTomato:Sec61β (See **Figures 3F** and **Figure 3 – Figure**
641 **Supplement C**). Quantification of boutons with complex (**C**) or simple (**D**) ER baskets
642 normalized to NMJ length. **(E)** WEKA segmentation of the ER (shown in magenta) of presynaptic
643 terminals. (**F**) Quantification of ER area fraction in control and *Atlastin* mutant boutons. (**G**)
644 Quantification of the mean intensity of the ER membrane marker tdTomato:Sec61β (within the
645 ER mask), normalized to wild-type control. (**D**, **E**) Graphs show mean +/- s.e.m. from 15 control
646 and 13 *Atlastin* mutant NMJs. **Associated with Figure 3 – Figure Supplement.**
647
648 **Figure 3 – Figure Supplement. *Atlastin* mutants have lower levels of the ER membrane**
649 **tdTomato: Sec61β at presynaptic terminals.** (**A**) Quantification of satellite boutons normalized
650 to total bouton number in control and *Atlastin* mutants. Representative maximum intensity
651 projection of a spinning disk confocal Z-stack from fixed larvae expressing the ER membrane
652 marker tdTomato:Sec61β (black) and stained with the neuronal marker HRP (magenta) in (**B**)
653 control and (**C**) *Atlastin* mutants. Neuronal outline is shown in blue. (**D**) Quantification of the
654 intensity of the ER membrane marker tdTomato:Sec61β, normalized to wild-type control. (**E**)

655 Coefficient of variation (CoV) of the ER membrane marker tdTomato:Sec61β. (**D**, **E**) Graphs
656 show mean +/- s.e.m. from 30 control and 30 *Atlastin* mutant NMJs.
657
658 **Figure 4. Luminal ER proteins are displaced to the cytosol in *Atlastin* mutants.** Maximum
659 projection of a Z-stack acquired live with an Airyscan microscope of control (**A**) and *Atlastin*
660 mutant (**B**) NMJs expressing the ER lumen marker BiP:sfGFP:HDEL. (**B**) *Atlastin* mutants exhibit
661 two distinct phenotypes at presynaptic terminals that were categorized as Phenotype A (**B, top**)
662 or Phenotype B (**B, bottom**). Control and *Atlastin* mutant images are contrast matched. (**C**) A
663 qualitative categorization of presynaptic terminals in control and *Atlastin* mutants exhibiting
664 "Phenotype A", "Phenotype B" or "no phenotype". (**D**) Histogram of normalized mean intensities
665 of the ER lumen marker BiP:sfGFP:HDEL. Displacement does not strongly correlate with steady-
666 state levels of BiP:sfGFP:HDEL. (**E**) Quantification of the intensity of the luminal ER marker
667 BiP:sfGFP:HDEL. (**F**) Coefficient of variation (CoV) of the luminal ER marker BiP:sfGFP:HDEL
668 in neurons of control and *Atlastin* mutant. (**E, F**) Graphs show mean +/- s.e.m. from 8 control
669 and 15 *Atlastin* mutant NMJs. Associated with **Figure 4 – Figure Supplement**.
670
671 **Figure 4 – Figure Supplement. Is and Ib motor neurons in various muscles and abdominal**
672 **segments of 3rd instar *Atlastin* mutant larvae exhibit similar cytosolic displacement of**
673 **BiP:sfGFP:HDEL.** Maximum projection of a live Airyscan Z-stack from larvae expressing the
674 ER lumen marker BiP:sfGFP:HDEL at muscle 12-13 (**A, left**) Muscle 6-7 (**A, right**); Muscle 4 in
675 segment A2 (**B, left**) and Muscle 4 in segment A4 (**B, right**).
676
677 **Figure 5. Luminal ER proteins are not displaced in other neuronal compartments or cell**
678 **types in *Drosophila* 3rd instar larvae.** All images were acquired by live Airyscan microscopy
679 from larvae expressing the ER lumen marker BiP:sfGFP:HDEL with Vglut-GAL4 (motor neurons)
680 or BG57-GAL4 (muscles). (**Left panel**) Maximum projection of a Z-stack of motor neuron axons.
681 (**Middle panel**) A single slice of motor neuron cell bodies. (**Right panel**) A single slice of body
682 wall muscles.
683
684 **Figure 6. The luminal displacement phenotype in *Atlastin* mutants is progressive.** (**A**)
685 Maximum intensity projections of a live Airyscan Z-stack acquired of 1st instar larvae expressing
686 the ER lumen marker BiP:sfGFP:HDEL (black) and stained with the neuronal marker HRP
687 (magenta). (**C**) A qualitative categorization of presynaptic terminals in control and *Atlastin* mutant

688 1st instar larvae expressing the ER lumen marker BiP:sfGFP:HDEL that exhibit “Phenotype A”,
689 “Phenotype B” or “No phenotype”. Data are shown from 16 control NMJs and 16 *Atlastin* mutant
690 NMJs.
691
692 **Figure 7. Luminal ER proteins displaced to the cytosol are sensitive to digitonin**
693 **treatment.** (**A**) Maximum projections of Z-stacks acquired live with a spinning disk confocal of
694 boutons expressing with Vglut-Gal4 GFP (control 1), BiP:sfGFP:HDEL (control 2),
695 BiP:sfGFP:HDEL in *Atlastin* mutants exhibiting Phenotype A and BiP:sfGFP:HDEL in Atlastin
696 mutants exhibiting Phenotype B. (**B**) Diagram of the expected distribution patterns before and
697 after digitonin treatment of cytosolic proteins and luminal ER proteins. Note that digitonin
698 treatment causes partial ER fragmentation. **(C)** Fractional change of fluorescence intensity at
699 presynaptic terminals expressing GFP (cytosolic protein) or BiP:sfGFP:HDEL in control and
700 *Atlastin* mutants following digitonin treatment. Graphs show mean +/- s.e.m. from 18 control and
701 20 *Atlastin* mutant NMJs. Statistical significance was only calculated between BiP:sfGFP:HDEL
702 samples since the baseline fluorescence and distribution of this marker was sensitive to digitonin
703 treatment in a manner distinct from cytosolic GFP.
704
705 **Movies S1-3.** Timelapse of maximum intensity projections from Airyscan Z-stacks of presynaptic
706 terminals expressing the ER membrane marker tdTomato:Sec61β. Images were acquired at a
707 frame rate of 0.65 frames per second and are played at a frame rate of 10 frames per second.
708 Scale bar is 1 μm.
709
710 **Movies S4-6.** Timelapse of maximum intensity projections from Airyscan Z-stacks of presynaptic
711 terminals expressing the ER lumen marker BiP:sfGFP:HDEL. Images were acquired at a frame
712 rate of 0.73 frames per second and are played at a frame rate of 10 frames per second. Scale
713 bar is 1 μm.
714

References:

Aponte-Santiago NA, Ormerod KG, Akbergenova Y, Littleton JT. 2020. Synaptic Plasticity Induced by Differential Manipulation of Tonic and Phasic Motoneurons in *Drosophila*. *J Neurosci* **40**:6270–6288. doi:10.1523/JNEUROSCI.0925-20.2020

Arganda-Carreras I, Kaynig V, Rueden C, Eliceiri KW, Schindelin J, Cardona A, Sebastian Seung H. 2017. Trainable Weka Segmentation: a machine learning tool for microscopy pixel classification. *Bioinformatics* **33**:2424–2426. doi:10.1093/bioinformatics/btx180

Blackstone C. 2018. Hereditary spastic paraplegia. *Handbook of Clinical Neurology,* **Vol. 148**:633–651. doi:10.1016/B978-0-444-64076-5.00041-7

Blackstone C. 2012. Cellular Pathways of Hereditary Spastic Paraplegia. *Annu Rev Neurosci* **35**:25–47. doi:10.1146/annurev-neuro-062111-150400

Blackstone C, O'Kane CJ, Reid E. 2011. Hereditary spastic paraplegias: membrane traffic and the motor pathway. *Nat Rev Neurosci* **12**:31–42. doi:10.1038/nrn2946

Boutry M, Morais S, Stevanin G. 2019. Update on the Genetics of Spastic Paraplegias. *Curr Neurol Neurosci Rep* **19**:18. doi:10.1007/s11910-019-0930-2

Burgoyne T, Patel S, Eden ER. 2015. Calcium signaling at ER membrane contact sites. *Biochimica et Biophysica Acta (BBA) - Molecular Cell Research*, 13th European Symposium on Calcium **1853**:2012–2017. doi:10.1016/j.bbamcr.2015.01.022

Carter SD, Hampton CM, Langlois R, Melero R, Farino ZJ, Calderon MJ, Li W, Wallace CT, Tran NH, Grassucci RA, Siegmund SE, Pemberton J, Morgenstern TJ, Eisenman L, Aguilar JI, Greenberg NL, Levy ES, Yi E, Mitchell WG, Rice WJ, Wigge C, Pilli J, George EW, Aslanoglou D, Courel M, Freyberg RJ, Javitch JA, Wills ZP, Area-Gomez E, Shiva S, Bartolini F, Volchuk A, Murray SA, Aridor M, Fish KN, Walter P, Balla T, Fass D, Wolf SG, Watkins SC, Carazo JM, Jensen GJ, Frank J, Freyberg Z. 2020. Ribosome-associated vesicles: A dynamic subcompartment of the endoplasmic reticulum in secretory cells. *Sci Adv* **6**:eaay9572. doi:10.1126/sciadv.aay9572

Chino H, Mizushima N. 2020. ER-Phagy: Quality Control and Turnover of Endoplasmic Reticulum. *Trends in Cell Biology* **30**:384–398. doi:10.1016/j.tcb.2020.02.001

Chouhan AK, Zhang J, Zinsmaier KE, Macleod GT. 2010. Presynaptic Mitochondria in Functionally Different Motor Neurons Exhibit Similar Affinities for Ca2+ But Exert Little Influence as Ca2+ Buffers at Nerve Firing Rates In Situ. *J Neurosci* **30**:1869–1881. doi:10.1523/JNEUROSCI.4701-09.2010

Christianson JC, Jarosch E, Sommer T. 2023. Mechanisms of substrate processing during ER-associated protein degradation. *Nat Rev Mol Cell Biol* 1–20. doi:10.1038/s41580-023-00633-8

Costantini LM, Fossati M, Francolini M, Snapp EL. 2012. Assessing the Tendency of Fluorescent Proteins to Oligomerize under Physiologic Conditions. *Traffic* **13**:643–649. doi:10.1111/j.1600-0854.2012.01336.x

Crapart C, Scott ZC, Konno T, Sharma A, Bailey DM, Avezov E, Koslover EF. 2023. Luminal transport rates through intact endoplasmic reticulum limit the magnitude of localized Ca2+ signals. doi:10.1101/2023.06.23.546357

de Juan-Sanz J, Holt GT, Schreiter ER, de Juan F, Kim DS, Ryan TA. 2017. Axonal Endoplasmic Reticulum Ca2+ Content Controls Release Probability in CNS Nerve Terminals. *Neuron* **93**:867-881.e6. doi:10.1016/j.neuron.2017.01.010

Del Signore SJ, Mitzner MG, Silveira AM, Fai TG, Rodal AA. 2022. An approach for quantitative mapping of synaptic periactive zone architecture and organization. *Mol Biol Cell* mbcE22080372. doi:10.1091/mbc.E22-08-0372

763 Deng C, Moradi M, Reinhard S, Ji C, Jablonka S, Hennlein L, Lüningschrör P, Doose S, Sauer
764 M, Sendtner M. 2021. Dynamic remodeling of ribosomes and endoplasmic reticulum in
765 axon terminals of motoneurons. *Journal of Cell Science* **134**:jcs258785.
766 doi:10.1242/jcs.258785
767 Deshpande M, Rodal AA. 2016. The Crossroads of Synaptic Growth Signaling, Membrane
768 Traffic and Neurological Disease: Insights from *Drosophila*: Synaptic Signaling and
769 Membrane Traffic in *Drosophila*. *Traffic* **17**:87–101. doi:10.1111/tra.12345
770 Espadas J, Pendin D, Bocanegra R, Escalada A, Misticoni G, Trevisan T, Velasco del Olmo A,
771 Montagna A, Bova S, Ibarra B, Kuzmin PI, Bashkirov PV, Shnyrova AV, Frolov VA,
772 Daga A. 2019. Dynamic constriction and fission of endoplasmic reticulum membranes
773 by reticulon. *Nat Commun* **10**:5327. doi:10.1038/s41467-019-13327-7
774 Feng Y, Ueda A, Wu C-F. 2004. A modified minimal hemolymph-like solution, HL3.1, for
775 physiological recordings at the neuromuscular junctions of normal and mutant
776 Drosophila larvae. *J Neurogenet* **18**:377–402. doi:10.1080/01677060490894522
777 Finsterer J, Löscher W, Quasthoff S, Wanschitz J, Auer-Grumbach M, Stevanin G. 2012.
778 Hereditary spastic paraplegias with autosomal dominant, recessive, X-linked, or
779 maternal trait of inheritance. *Journal of the Neurological Sciences* **318**:1–18.
780 doi:10.1016/j.jns.2012.03.025
781 Fowler PC, Garcia-Pardo ME, Simpson JC, O'Sullivan NC. 2019. NeurodegenERation: The
782 Central Role for ER Contacts in Neuronal Function and Axonopathy, Lessons From
783 Hereditary Spastic Paraplegias and Related Diseases. *Front Neurosci* **13**.
784 doi:10.3389/fnins.2019.01051
785 Friedman JR, Lackner LL, West M, DiBenedetto JR, Nunnari J, Voeltz GK. 2011. ER tubules
786 mark sites of mitochondrial division. *Science* **334**:358–362.
787 doi:10.1126/science.1207385
788 Glock C, Biever A, Tushev G, Nassim-Assir B, Kao A, Bartnik I, tom Dieck S, Schuman EM.
789 2021. The translatome of neuronal cell bodies, dendrites, and axons. *Proceedings of*
790 *the National Academy of Sciences* **118**:e2113929118. doi:10.1073/pnas.2113929118
791 Graf ER, Heerssen HM, Wright CM, Davis GW, DiAntonio A. 2011. Stathmin is Required for
792 Stability of the Drosophila Neuromuscular Junction. *J Neurosci* **31**:15026–15034.
793 doi:10.1523/JNEUROSCI.2024-11.2011
794 Gregorio CD, Delgado R, Ibacache A, Sierralta J, Couve A. 2017. Drosophila Atlastin in motor
795 neurons is required for locomotion and presynaptic function. *J Cell Sci* **130**:3507–3516.
796 doi:10.1242/jcs.201657
797 Holcman D, Parutto P, Chambers JE, Fantham M, Young LJ, Marciniak SJ, Kaminski CF, Ron
798 D, Avezov E. 2018. Single particle trajectories reveal active endoplasmic reticulum
799 luminal flow. *Nat Cell Biol* **20**:1118–1125. doi:10.1038/s41556-018-0192-2
800 Hoyer MJ, Chitwood PJ, Ebmeier CC, Striepen JF, Qi RZ, Old WM, Voeltz GK. 2018. A Novel
801 Class of ER Membrane Proteins Regulates ER-Associated Endosome Fission. *Cell*
802 **175**:254-265.e14. doi:10.1016/j.cell.2018.08.030
803 Hu J, Shibata Y, Zhu P-P, Voss C, Rismanchi N, Prinz WA, Rapoport TA, Blackstone C. 2009.
804 A Class of Dynamin-like GTPases Involved in the Generation of the Tubular ER
805 Network. *Cell* **138**:549–561. doi:10.1016/j.cell.2009.05.025
806 Hu X, Wu F, Sun S, Yu W, Hu J. 2015. Human atlastin GTPases mediate differentiated fusion
807 of endoplasmic reticulum membranes. *Protein Cell* **6**:307–311. doi:10.1007/s13238-
808 015-0139-3
809 King C, Sengupta P, Seo AY, Lippincott-Schwartz J. 2020. ER membranes exhibit phase
810 behavior at sites of organelle contact. *Proceedings of the National Academy of*
811 *Sciences* **117**:7225–7235. doi:10.1073/pnas.1910854117

Le Gall S, Neuhof A, Rapoport T. 2004. The Endoplasmic Reticulum Membrane Is Permeable to Small Molecules. *MBoC* **15**:447–455. doi:10.1091/mbc.e03-05-0325

Lee M, Paik SK, Lee M-J, Kim Y-J, Kim S, Nahm M, Oh S-J, Kim H-M, Yim J, Lee CJ, Bae YC, Lee S. 2009. Drosophila Atlastin regulates the stability of muscle microtubules and is required for synapse development. *Developmental Biology* **330**:250–262. doi:10.1016/j.ydbio.2009.03.019

Liu X, Guo X, Niu L, Li X, Sun F, Hu J, Wang X, Shen K. 2019. Atlastin-1 regulates morphology and function of endoplasmic reticulum in dendrites. *Nat Commun* **10**:1–15. doi:10.1038/s41467-019-08478-6

Lu L, Ladinsky MS, Kirchhausen T. 2009. Cisternal Organization of the Endoplasmic Reticulum during Mitosis. *MBoC* **20**:3471–3480. doi:10.1091/mbc.e09-04-0327

Lü L, Niu L, Hu J. 2020. “At last in” the physiological roles of the tubular ER network. *Biophys Rep* **6**:105–114. doi:10.1007/s41048-020-00113-y

Lu M, Tartwijk FW van, Lin JQ, Nijenhuis W, Parutto P, Fantham M, Christensen CN, Avezov E, Holt CE, Tunnacliffe A, Holcman D, Kapitein L, Schierle GSK, Kaminski CF. 2020. The structure and global distribution of the endoplasmic reticulum network are actively regulated by lysosomes. *Science Advances* **6**:eabc7209. doi:10.1126/sciadv.abc7209

McKibbin C, Mares A, Piacenti M, Williams H, Roboti P, Puumalainen M, Callan AC, Lesiak-Mieczkowska K, Linder S, Harant H, High S, Flitsch SL, Whitehead RC, Swanton E. 2012. Inhibition of protein translocation at the endoplasmic reticulum promotes activation of the unfolded protein response. *Biochemical Journal* **442**:639–648. doi:10.1042/BJ20111220

Niu L, Ma T, Yang F, Yan B, Tang X, Yin H, Wu Q, Huang Y, Yao Z-P, Wang J, Guo Y, Hu J. 2019. Atlastin-mediated membrane tethering is critical for cargo mobility and exit from the endoplasmic reticulum. *PNAS* **116**:14029–14038. doi:10.1073/pnas.1908409116

Obara CJ, Nixon-Abell J, Moore AS, Riccio F, Hoffman DP, Shtengel G, Xu CS, Schaefer K, Pasolli HA, Masson J-B, Hess HF, Calderon CP, Blackstone C, Lippincott-Schwartz J. 2022. Motion of single molecular tethers reveals dynamic subdomains at ER-mitochondria contact sites. doi:10.1101/2022.09.03.505525

Oliva MK, Pérez-Moreno JJ, O’Shaughnessy J, Wardill TJ, O’Kane CJ. 2020. Endoplasmic Reticulum Lumenal Indicators in Drosophila Reveal Effects of HSP-Related Mutations on Endoplasmic Reticulum Calcium Dynamics. *Front Neurosci* **14**. doi:10.3389/fnins.2020.00816

Orso G, Pendin D, Liu S, Tosetto J, Moss TJ, Faust JE, Micaroni M, Egorova A, Martinuzzi A, McNew JA, Daga A. 2009. Homotypic fusion of ER membranes requires the dynamin-like GTPase Atlastin. *Nature* **460**:978–983. doi:10.1038/nature08280

O’Sullivan NC, Jahn TR, Reid E, O’Kane CJ. 2012. Reticulon-like-1, the Drosophila orthologue of the Hereditary Spastic Paraplegia gene reticulon 2, is required for organization of endoplasmic reticulum and of distal motor axons. *Hum Mol Genet* **21**:3356–3365. doi:10.1093/hmg/dds167

Özkan N, Koppers M, van Soest I, van Harten A, Jurriens D, Liv N, Klumperman J, Kapitein LC, Hoogenraad CC, Farías GG. 2021. ER - lysosome contacts at a pre-axonal region regulate axonal lysosome availability. *Nat Commun* **12**:4493. doi:10.1038/s41467-021-24713-5

Öztürk Z, O’Kane CJ, Pérez-Moreno JJ. 2020. Axonal Endoplasmic Reticulum Dynamics and Its Roles in Neurodegeneration. *Frontiers in Neuroscience* **14**:1–33. doi:10.3389/fnins.2020.00048

Perez-Alvarez A, Yin S, Schulze C, Hammer JA, Wagner W, Oertner TG. 2020. Endoplasmic reticulum visits highly active spines and prevents runaway potentiation of synapses. *Nature Communications* **11**:5083. doi:10.1038/s41467-020-18889-5

Pérez-Moreno JJ, Smith RC, Oliva MK, Gallo F, Ojha S, Müller KH, O'Kane CJ. 2023. Drosophila SPG12 ortholog, reticulon-like 1, governs presynaptic ER organization and Ca2+ dynamics. *J Cell Biol* **222**:e202112101. doi:10.1083/jcb.202112101

Raffaello A, Mammucari C, Gherardi G, Rizzuto R. 2016. Calcium at the Center of Cell Signaling: Interplay between Endoplasmic Reticulum, Mitochondria, and Lysosomes. *Trends in Biochemical Sciences* **41**:1035–1049. doi:10.1016/j.tibs.2016.09.001

Raiborg C, Wenzel EM, Pedersen NM, Olsvik H, Schink KO, Schultz SW, Vietri M, Nisi V, Bucci C, Brech A, Johansen T, Stenmark H. 2015. Repeated ER–endosome contacts promote endosome translocation and neurite outgrowth. *Nature* **520**:234–238. doi:10.1038/nature14359

Rao K, Stone MC, Weiner AT, Gheres KW, Zhou C, Deitcher DL, Levitan ES, Rolls MM. 2016. Spastin, atlastin, and ER relocalization are involved in axon but not dendrite regeneration. *MBoC* **27**:3245–3256. doi:10.1091/mbc.E16-05-0287

Rismanchi N, Soderblom C, Stadler J, Zhu P-P, Blackstone C. 2008. Atlastin GTPases are required for Golgi apparatus and ER morphogenesis. *Hum Mol Genet* **17**:1591–1604. doi:10.1093/hmg/ddn046

Rowland AA, Chitwood PJ, Phillips MJ, Voeltz GK. 2014. ER Contact Sites Define the Position and Timing of Endosome Fission. *Cell* **159**:1027–1041. doi:10.1016/j.cell.2014.10.023

Schwarz DS, Blower MD. 2016. The endoplasmic reticulum: structure, function and response to cellular signaling. *Cell Mol Life Sci* **73**:79–94. doi:10.1007/s00018-015-2052-6

Scott ZC, Brown AI, Mogre SS, Westrate LM, Koslover EF. 2021. Diffusive search and trajectories on tubular networks: a propagator approach. *Eur Phys J E* **44**:80. doi:10.1140/epje/s10189-021-00083-0

Snow PM, Patel NH, Harrelson AL, Goodman CS. 1987. Neural-specific carbohydrate moiety shared by many surface glycoproteins in Drosophila and grasshopper embryos. *J Neurosci* **7**:4137–4144. doi:10.1523/JNEUROSCI.07-12-04137.1987

Spits M, Neefjes J. 2021. Mobile late endosomes modulate peripheral endoplasmic reticulum network architecture. *EMBO reports* **22**:e50815. doi:10.15252/embr.202050815

Subramanian K, Meyer T. 1997. Calcium-Induced Restructuring of Nuclear Envelope and Endoplasmic Reticulum Calcium Stores. *Cell* **89**:963–971. doi:10.1016/S0092-8674(00)80281-0

Summerville JB, Faust JF, Fan E, Pendin D, Daga A, Formella J, Stern M, McNew JA. 2016. The effects of ER morphology on synaptic structure and function in Drosophila melanogaster. *J Cell Sci* **129**:1635–1648. doi:10.1242/jcs.184929

Sun L, Yu F, Ullah A, Hubrack S, Daalis A, Jung P, Machaca K. 2011. Endoplasmic Reticulum Remodeling Tunes IP3-Dependent Ca2+ Release Sensitivity. *PLOS ONE* **6**:e27928. doi:10.1371/journal.pone.0027928

Thevenaz P, Ruttimann UE, Unser M. 1998. A pyramid approach to subpixel registration based on intensity. *IEEE Trans on Image Process* **7**:27–41. doi:10.1109/83.650848

Wang X, Olberding KE, White C, Li C. 2011. Bcl-2 proteins regulate ER membrane permeability to luminal proteins during ER stress-induced apoptosis. *Cell Death Differ* **18**:38–47. doi:10.1038/cdd.2010.68

Wu Y, Whiteus C, Xu CS, Hayworth KJ, Weinberg RJ, Hess HF, Camilli PD. 2017. Contacts between the endoplasmic reticulum and other membranes in neurons. *PNAS* **114**:E4859–E4867. doi:10.1073/pnas.1701078114

907 Yalçın B, Zhao L, Stofanko M, O'Sullivan NC, Kang ZH, Roost A, Thomas MR, Zaessinger S,
908 Blard O, Patto AL, Sohail A, Baena V, Terasaki M, O'Kane CJ. 2017. Modeling of
909 axonal endoplasmic reticulum network by spastic paraplegia proteins. *eLife* **6**:1–27.
910 doi:10.7554/eLife.23882
911 Zamponi E, Meehl JB, Voeltz GK. 2022. The ER ladder is a unique morphological feature of
912 developing mammalian axons. *Dev Cell* **57**:1369-1382.e6.
913 doi:10.1016/j.devcel.2022.05.002
914 Zhu P-P, Hung H-F, Batchenkova N, Nixon-Abell J, Henderson J, Zheng P, Renvoisé B, Pang
915 S, Xu CS, Saalfeld S, Funke J, Xie Y, Svara F, Hess HF, Blackstone C. 2022.
916 Transverse endoplasmic reticulum expansion in hereditary spastic paraplegia
917 corticospinal axons. *Hum Mol Genet* **31**:2779–2795. doi:10.1093/hmg/ddac072
918 Zhu P-P, Soderblom C, Tao-Cheng J-H, Stadler J, Blackstone C. 2006. SPG3A protein
919 atlastin-1 is enriched in growth cones and promotes axon elongation during neuronal
920 development. *Hum Mol Genet* **15**:1343–1353. doi:10.1093/hmg/ddl054
921

922

923

Figure 1

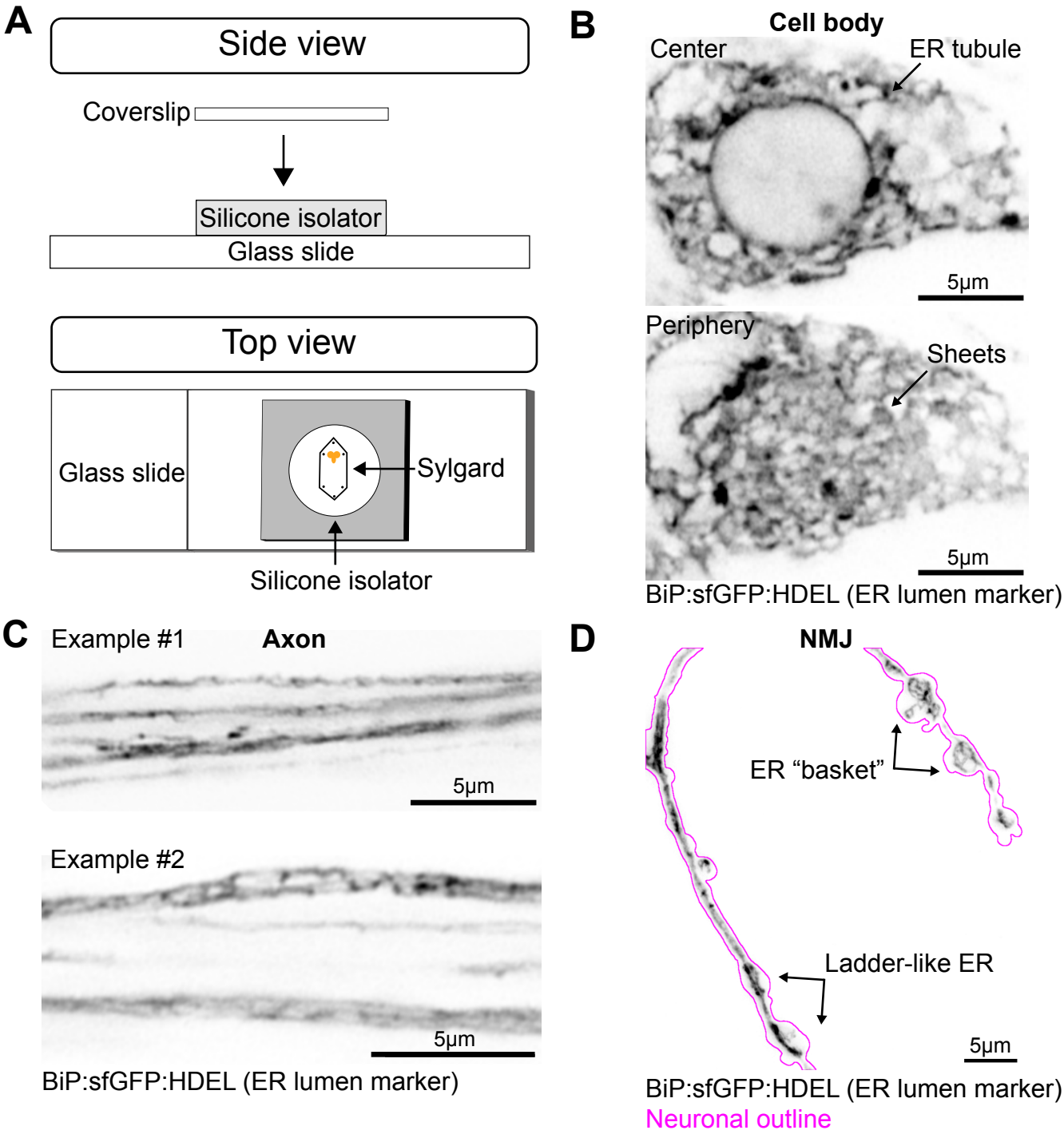
A
Side view
Coverslip
Silicone isolator
Glass slide
Top view
Glass slide
Sylgard
Silicone isolator
B
Cell body
Center
ER tubule
5μm
Periphery
Sheets
5μm
BiP:sfGFP:HDEL (ER lumen marker)
C
Example #1
Axon
5μm
Example #2
5μm
BiP:sfGFP:HDEL (ER lumen marker)
D
NMJ
ER "basket"
Ladder-like ER
5μm
BiP:sfGFP:HDEL (ER lumen marker)
Neuronal outline

Figure 2

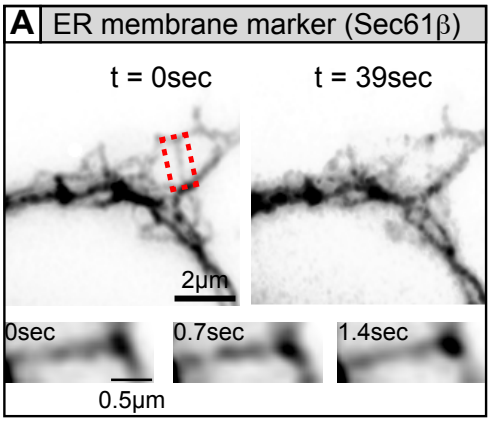

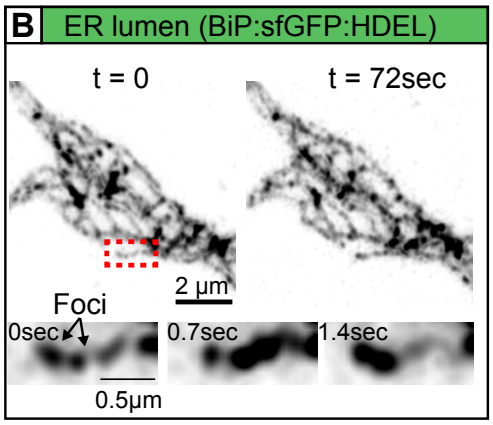

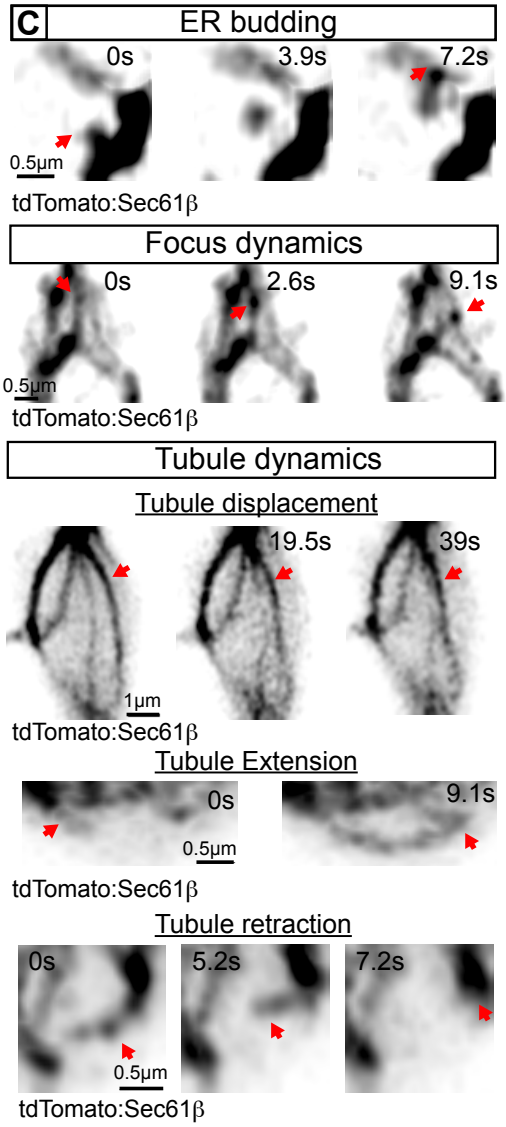

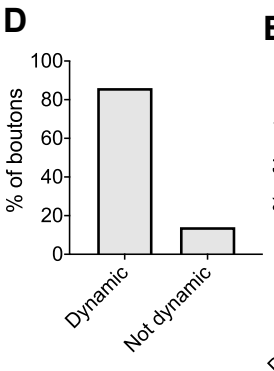

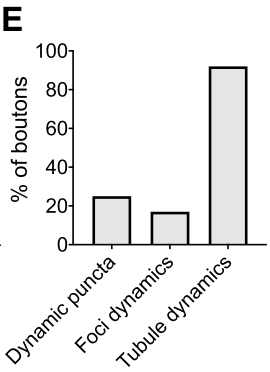

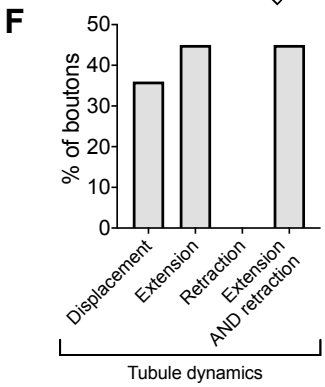

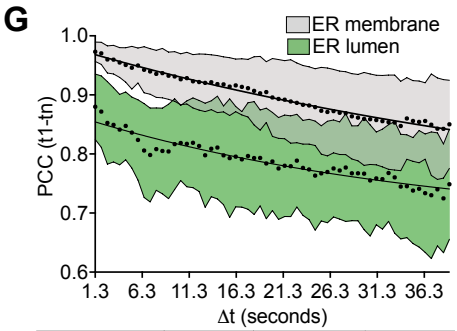

	K (1/s)	Half-life (s)	Tau (s)
ER membrane	0.01618	42.85	61.82
ER lumen	0.02697	25.70	37.08

Figure 3

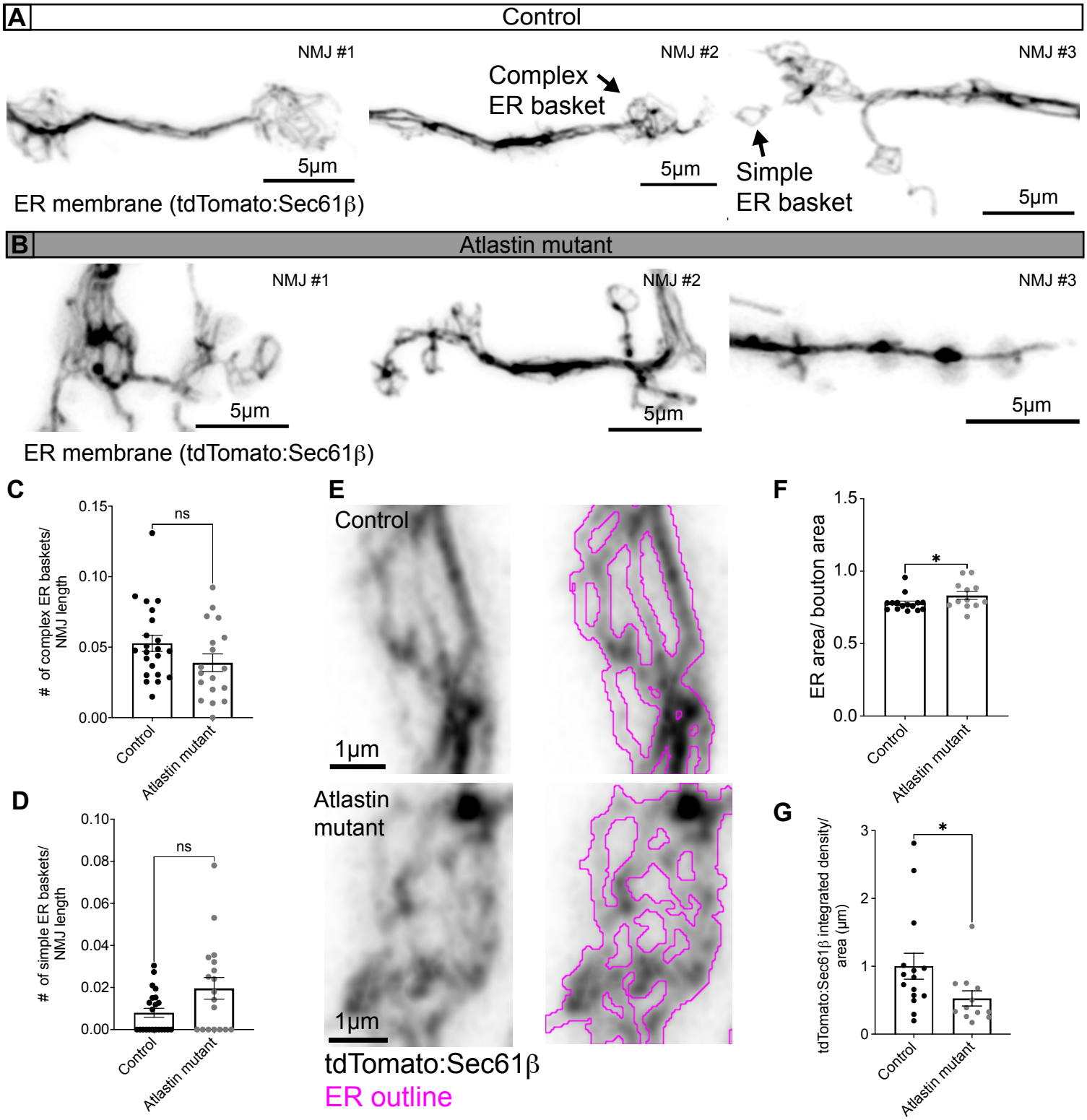
A
Control
NMJ #1
NMJ #2
NMJ #3
Complex
ER basket
Simple
ER basket
5μm
5μm
5μm
ER membrane (tdTomato:Sec61β)
B
Atlastin mutant
NMJ #1
NMJ #2
NMJ #3
5μm
5μm
5μm
ER membrane (tdTomato:Sec61β)
C
# of complex ER baskets/ NMJ length
0.15
0.10
0.05
0.00
ns
Control
Atlastin mutant
D
# of simple ER baskets/ NMJ length
0.10
0.08
0.06
0.04
0.02
0.00
ns
Control
Atlastin mutant
E
Control
1μm
Atlastin mutant
1μm
tdTomato:Sec61β
ER outline
F
ER area/ bouton area
1.5
1.0
0.5
0.0
*
Control
Atlastin mutant
G
tdTomato:Sec61β integrated density/ area (μm)
3
2
1
0
*
Control
Atlastin mutant

Figure 3-Supplement

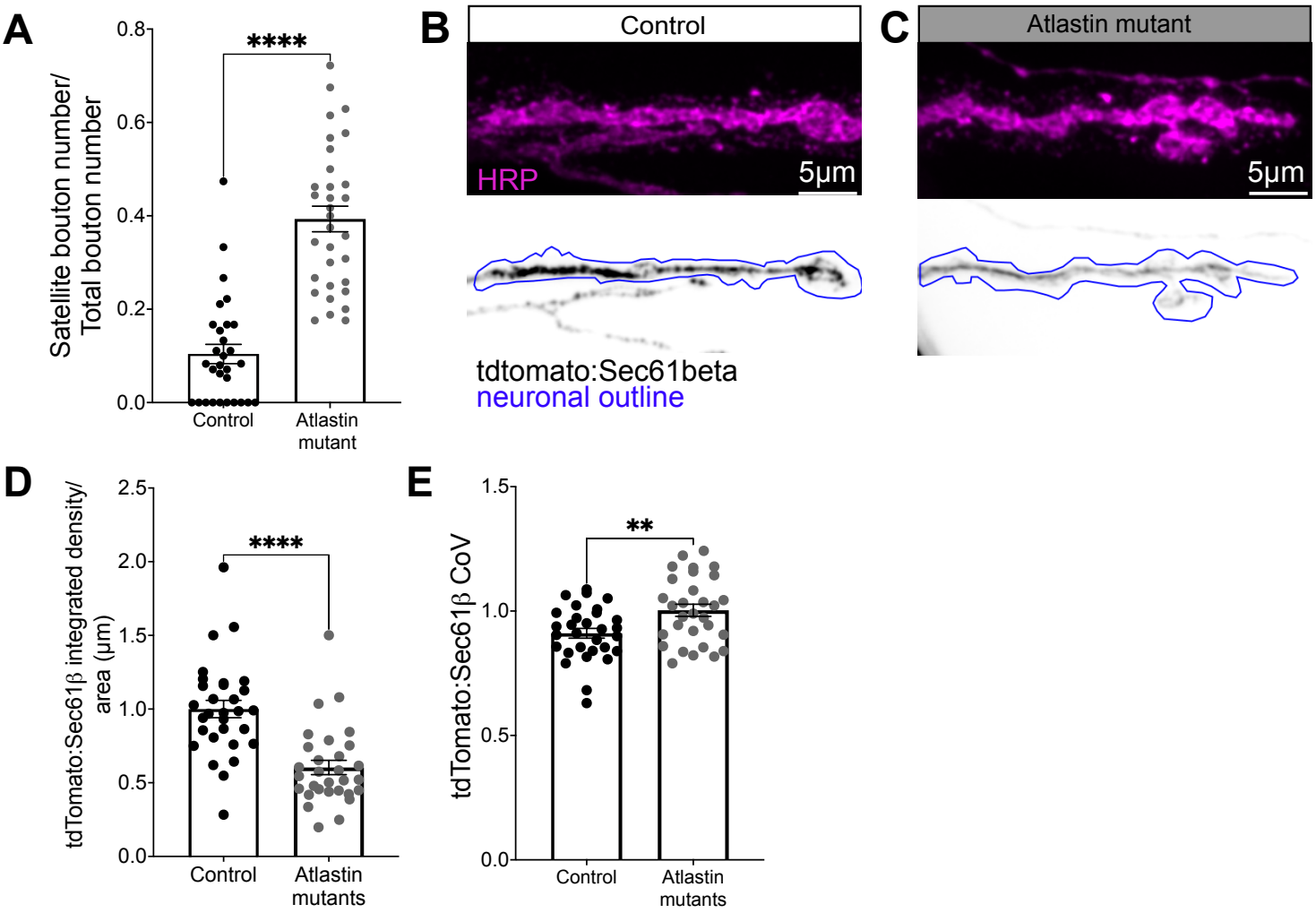

Figure 4

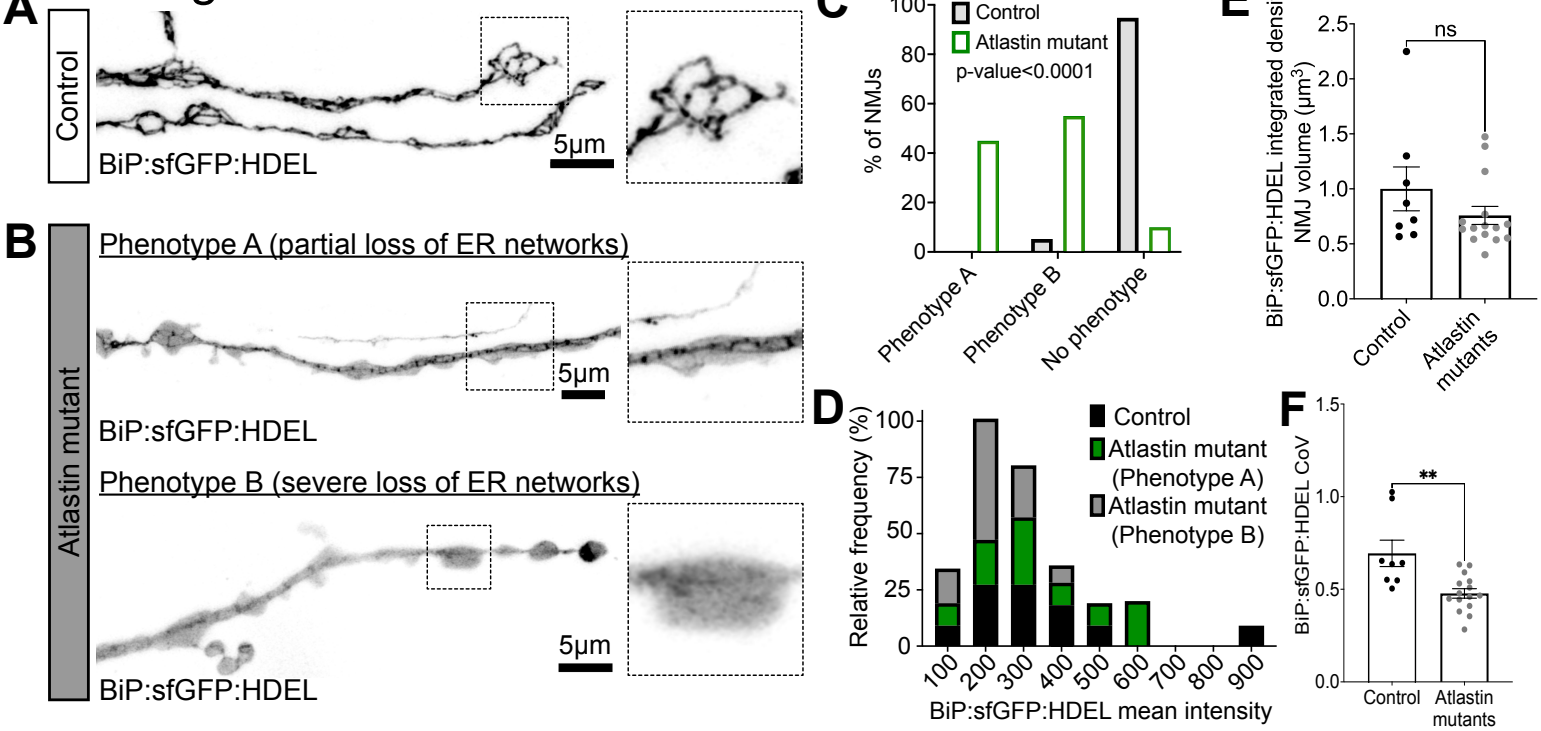
A
Control
5µm
BiP:sfGFP:HDEL
B
Atlastin mutant
Phenotype A (partial loss of ER networks)
5µm
BiP:sfGFP:HDEL
Phenotype B (severe loss of ER networks)
5µm
BiP:sfGFP:HDEL
C
Control
Atlastin mutant
p-value<0.0001
% of NMJs
Phenotype A
Phenotype B
No phenotype
D
Control
Atlastin mutant (Phenotype A)
Atlastin mutant (Phenotype B)
Relative frequency (%)
BiP:sfGFP:HDEL mean intensity
E
ns
BiP:sfGFP:HDEL integrated density/ NMJ volume (µm³)
Control
Atlastin mutants
F
**
BiP:sfGFP:HDEL CoV
Control
Atlastin mutants

Figure 4-Supplement

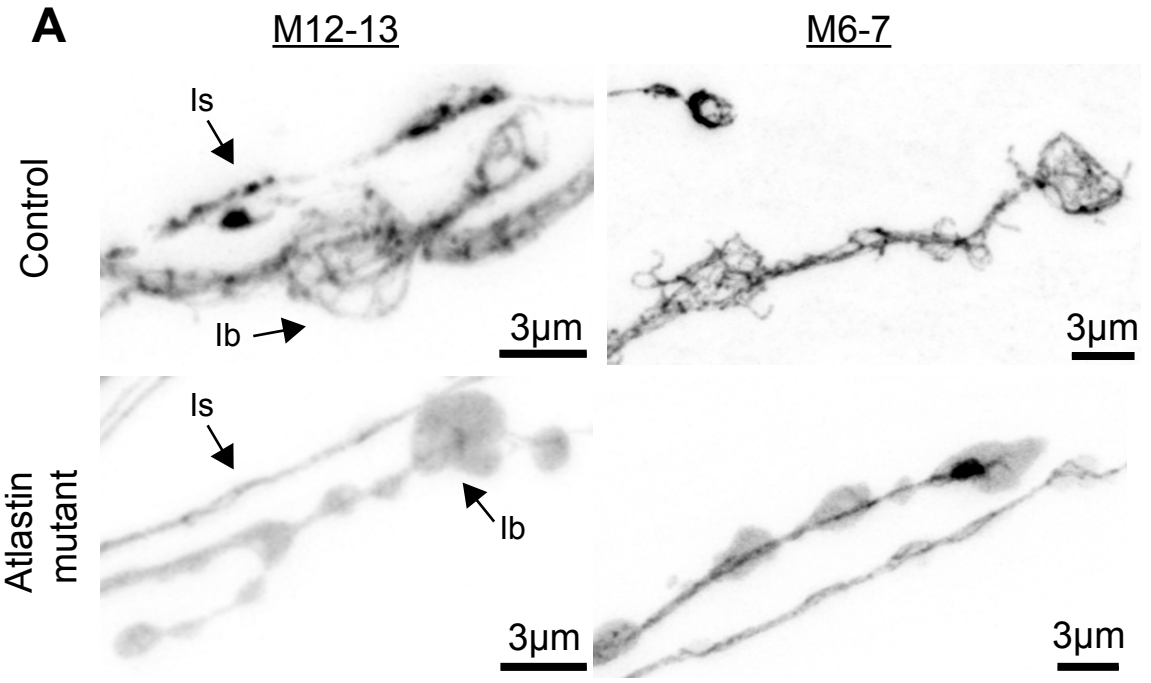

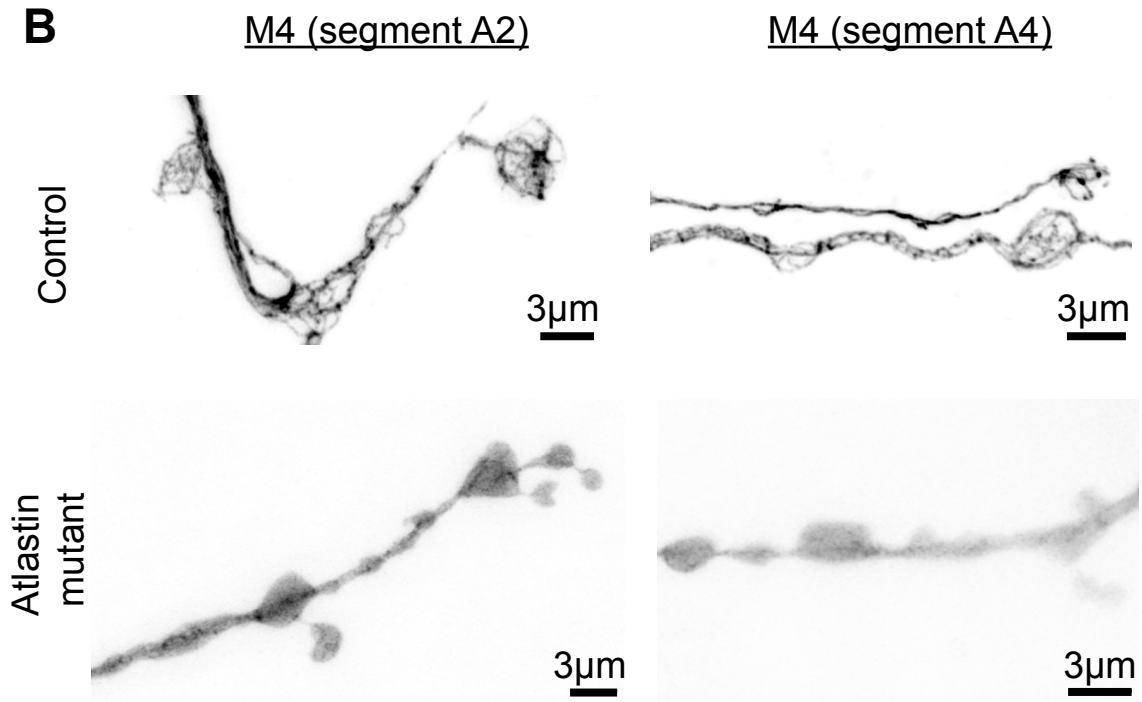

Figure 5

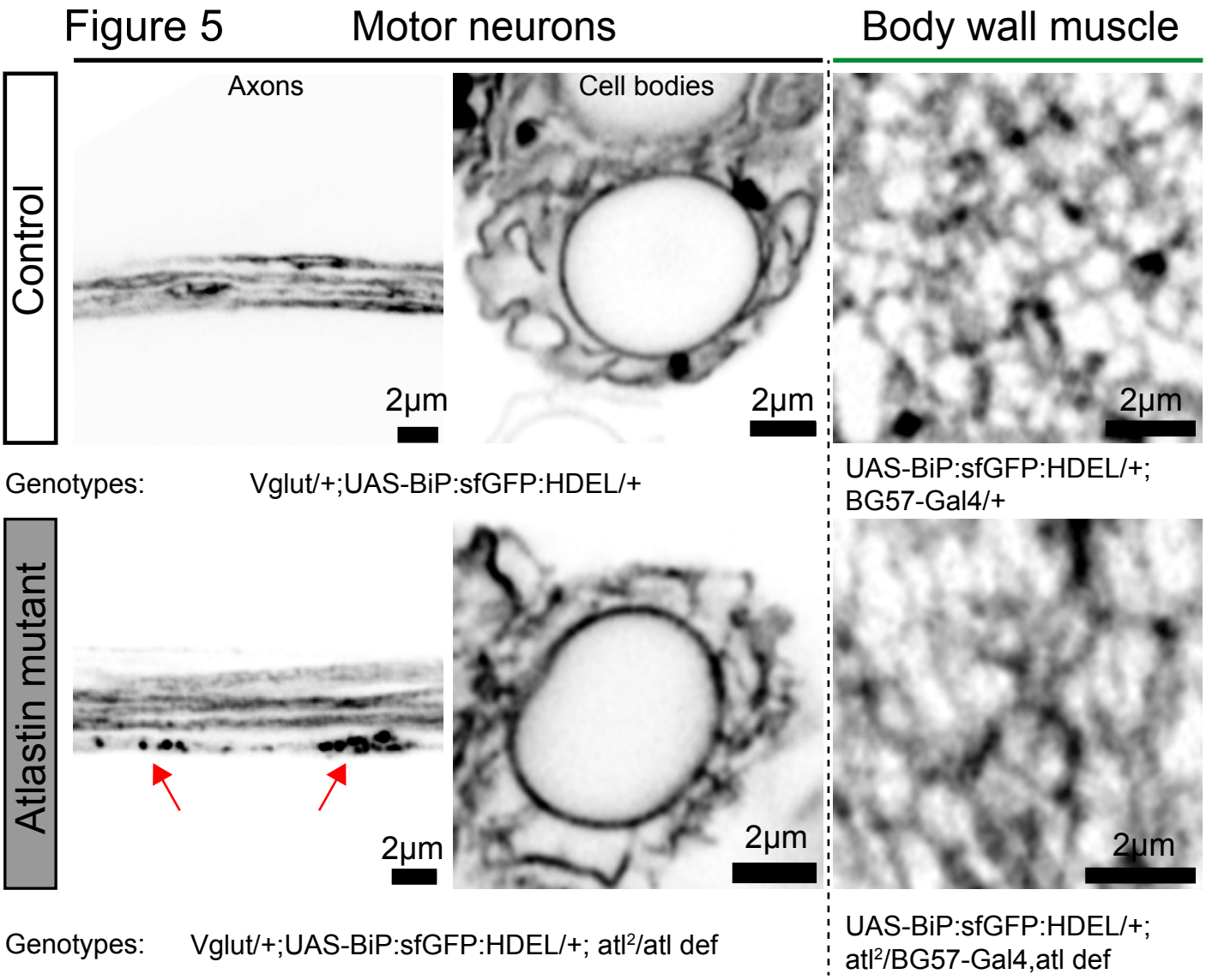
Motor neurons
Body wall muscle
Control
Axons
Cell bodies
2µm
2µm
2µm
Genotypes:
Vglut/+;UAS-BiP:sfGFP:HDEL/+
UAS-BiP:sfGFP:HDEL/+;
BG57-Gal4/+
Atlastin mutant
2µm
2µm
2µm
Genotypes:
Vglut/+;UAS-BiP:sfGFP:HDEL/+; atl²/atl def
UAS-BiP:sfGFP:HDEL/+;
atl²/BG57-Gal4,atl def

Figure 6

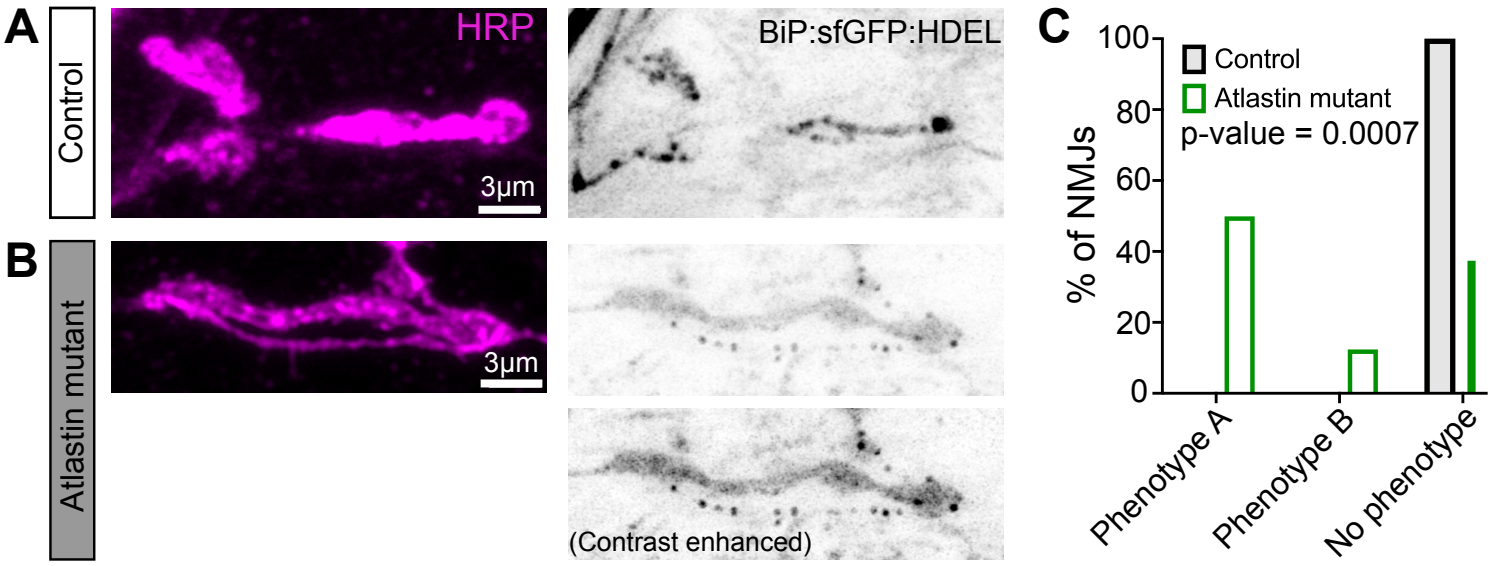
A
Control
HRP
3μm
BiP:sfGFP:HDEL
B
Atlastin mutant
3μm
(Contrast enhanced)
C
Control
Atlastin mutant
p-value = 0.0007
% of NMJs
100
80
60
40
20
0
Phenotype A
Phenotype B
No phenotype

Figure 7

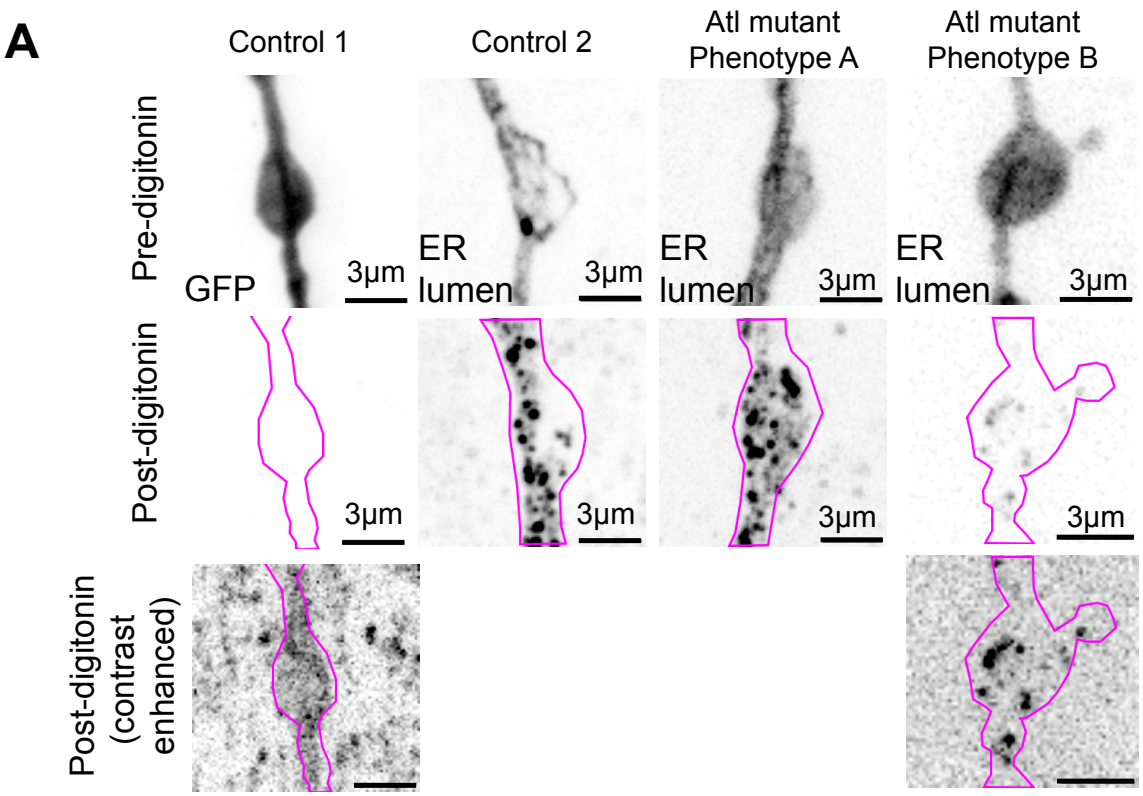
A
Control 1
Control 2
Atl mutant Phenotype A
Atl mutant Phenotype B
Pre-digitonin
Post-digitonin
Post-digitonin (contrast enhanced)
GFP
ER lumen
3µm

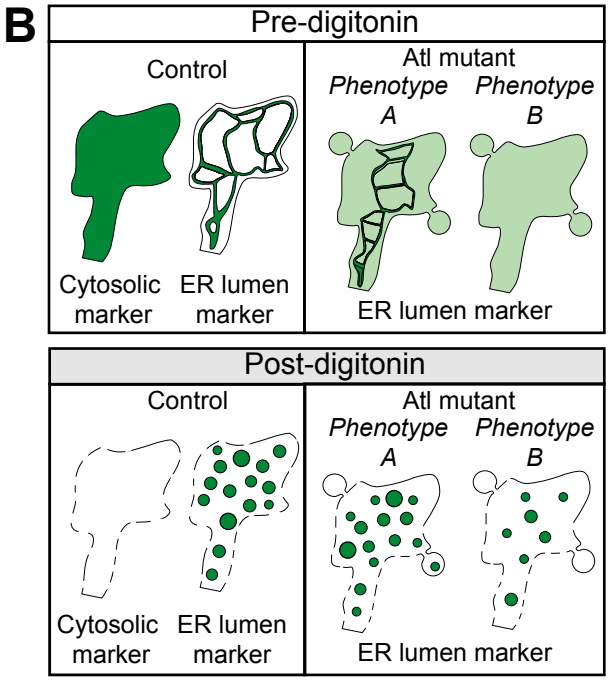
B
Pre-digitonin
Control
Atl mutant
Phenotype A
Phenotype B
Cytosolic marker
ER lumen marker
ER lumen marker
Post-digitonin
Control
Atl mutant
Phenotype A
Phenotype B
Cytosolic marker
ER lumen marker
ER lumen marker

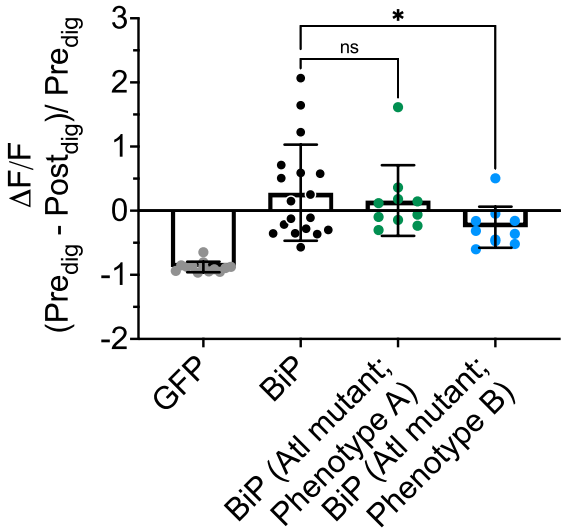
C
ΔF/F
(Pre_dig - Post_dig)/ Pre_dig
3
2
1
0
-1
-2
*
ns
GFP
BiP
BiP (Atl mutant; Phenotype A)
BiP (Atl mutant; Phenotype B)

Table S1 – Detailed genotypes and statistics reporting

Experiments were done at muscle 4 unless otherwise noted
All analyses were performed in Fiji
A: Pearson's correlation coefficient over time
B: Mean intensity of marker
C: CoV

Figure	Genotype/Conditions	N	Measurement	Statistical Test(s)
Figure 2D-G Dynamics of ER luminal and membrane markers Airyscan	ER lumen: Vglut/+;UAS-BiP:sfGFP:HDEL/+ ER Membrane: Vglut/+;;UAS-tdTomato:Sec61β/+	2 larvae/ 10 boutons (segment A3) 4 larvae/14 boutons (segments A2-A5)	ER dynamics A	No statistics
Figure 3C,D Complex and simple ER network structure analysis Airyscan	Control: Vglut/+;UAS-tdTomato:Sec61β/+ *Atlastin* mutant: Vglut/+;UAS-tdTomato:Sec61β/+;atl^2/atl def	4 larvae/14 NMJs (segments A2-A5) 4 larvae/11 NMJs (segments A2-A5)	Qualitative analysis of ER network structure in boutons expressing tdTomato:Sec61β	Figure 3C: Unpaired Mann-Whitney test, P<0.0001 Figure 3D: Unpaired Mann-Whitney test, P<0.0001
Figure 3 F,G ER network structure bouton analysis	Control: Vglut/+;UAS-tdTomato:Sec61β/+	4 larvae/15 boutons (segments A2-A5)	ER network per bouton area and Sec61β levels B, C	Figure 3F: Unpaired Mann-Whitney test, P<0.0001

	Atlastin mutant: Vglut/+;UAS-tdTomato:Sec61β/+;atl^2/atl def	4 larvae/ 13 boutons (segments A2-A5)		Figure 3G: Unpaired Mann-Whitney test, P<0.0001
Figure 3 – Figure Supplement (A)	Control: Vglut/+;UAS-tdTomato:Sec61β/+ *Atlastin* mutant: Vglut/+;UAS-tdTomato:Sec61β/+;atl^2/atl def	8 larvae/ 30 NMJs (segments A2- A5) 8 larvae/ 30 NMJs (segments A2-A5)	Count of satellite boutons	Figure 3 – Figure Supplement (A): Unpaired Mann-Whitney test, P<0.0001
Figure 3 – Figure Supplement (D-E) Overall levels of ER membrane markers at nerve terminals Spinning disk	Control: Vglut/+;UAS-tdTomato:Sec61β/+ *Atlastin* mutant: Vglut/+;UAS-tdTomato:Sec61β/+;atl^2/atl def	8 larva/ 30 NMJs (segments A2- A5) 8 larva/ 30 NMJs (segments A2-A5)	Sec61β levels B, C	Figure 3 – Figure Supplement (D): Unpaired Mann-Whitney test, P<0.0001 Figure 3 – Figure Supplement (E): Unpaired t-test, P<0.05
Figure 4C Categorization of ER network phenotypes in *Atlastin* mutants expressing luminal ER markers Airyscan	Control: Vglut/+;UAS-BiP:sfGFP:HDEL/+ *Atlastin* mutant: Vglut/+; UAS-BiP:sfGFP:HDEL/+;atl^2/atl def	6 larvae/ 21 NMJs (Segments A2-A5) 8 larvae/ 22 NMJs (Segments A2-A5)	Categories: - Phenotype A - Phenotype B No phenotype	Chi-square, P<0.0001

Figure 4D-F Overall levels of ER lumen markers at nerve terminals of *Atlastin* mutants Airyscan	Control: Vglut/+;UAS-BiP:sfGFP:HDEL/+ *Atlastin* mutant: Vglut/+; UAS-BiP:sfGFP:HDEL/+;atl^2/atl def	2 larvae/ 8 NMJs (Segments A2-A5) 4 larvae/ 15 NMJs (Segments A2-A5)	BiP:sfGFP:HDEL levels B,C	Figure 4E: Unpaired Mann-Whitney test, P<0.0001 Figure 4F: Unpaired t-test, P<0.05
Figure 6C Categorization of ER network phenotypes in1st instar larvae *Atlastin* mutants expressing a luminal ER marker Airyscan	Control: Vglut/+;UAS-BiP:sfGFP:HDEL/+ *Atlastin* mutant: Vglut/+; UAS-BiP:sfGFP:HDEL/+;atl^2/atl def	7 larvae/ 16 NMJs (Segments A4-A5) 6 larvae/ 16NMJs (Segments A4-A5)	Categories: - Phenotype A - Phenotype B - No phenotype	Chi-square, P<0.0001
Figure 7C Mean intensity of luminal ER markers with digitonin treatment Spinning disk	Control1: Vglut/+;UAS-GFP/+ Control2: Vglut/+;UAS-BiP:sfGFP:HDEL/+ *Atlastin* mutant: Vglut/+; UAS-BiP:sfGFP:HDEL/+;atl^2/atl def	4 larvae/ 13NMJs (Segments A4-A5) 5 larvae/ 18 NMJs (Segments A4-A5) 5 larvae/ 20 NMJs (Segments A4-A5)	Change in fluorescence before and after digitonin treatment	Non-parametric One-way ANOVA for BiP samples only (Kruskal-Wallis test), P<0.0001